

000 PSDNORM: TEMPORAL NORMALIZATION FOR DEEP 001 002 LEARNING IN SLEEP STAGING 003 004

005 **Anonymous authors**

006 Paper under double-blind review

007 008 ABSTRACT 009

010 Distribution shift poses a significant challenge in machine learning, particularly in
011 biomedical applications using data collected across different subjects, institutions,
012 and recording devices, such as sleep data. While existing normalization layers,
013 BatchNorm, LayerNorm and InstanceNorm, help mitigate distribution shifts, when
014 applied over the time dimension they ignore the dependencies and auto-correlation
015 inherent to the vector coefficients they normalize. In this paper, we propose
016 PSDNorm that leverages Monge mapping and temporal context to normalize feature
017 maps in deep learning models for signals. Evaluations with architectures based on
018 U-Net or transformer backbones trained on 10K subjects across 10 datasets, show
019 that PSDNorm achieves state-of-the-art performance on unseen left-out datasets
020 while being [more robust to data scarcity](#).
021
022

023 1 INTRODUCTION 024

025 **Data Shift in Physiological Signals** Machine learning techniques have achieved remarkable
026 success in various domains, including computer vision, biology, audio processing, and language
027 understanding. However, these methods face significant challenges when there are distribution shifts
028 between training and evaluation datasets (Moreno-Torres et al., 2012). For example, in biological
029 data, such as electroencephalography (EEG) signals, the distribution of the data can vary significantly.
030 Indeed, data is collected from different subjects, electrode positions, and recording conditions.
031 This paper focuses on sleep staging, a clinical task that consists in classifying periods of sleep in
032 different stages based on EEG signals (Stevens & Clark, 2004). Depending on the dataset, the
033 cohort can be composed of different age groups, sex repartition, health conditions, and recording
034 conditions (O'Reilly et al., 2014; Quan et al., 1998; Marcus et al., 2013). Such variability brings shift
035 in the distribution making it challenging for the model to generalize to unseen datasets.
036

037 **Normalization to Address Data Shift** Normalization layers are widely used in deep learning to
038 improve training stability and generalization. Common layers include BatchNorm (Ioffe & Szegedy,
039 2015), LayerNorm (Ba et al., 2016), and InstanceNorm (Ulyanov, 2016), which respectively compute
040 statistics across the batch, normalize across all features within each sample, and normalize each
041 channel independently within a sample. Some normalization methods target specific tasks, such as
042 EEG covariance matrices (Kobler et al., 2022) or time-series forecasting (Kim et al., 2021), but they
043 do not fully address spectral distribution shifts reflected in the temporal auto-correlations of signals.
044

045 [Other papers have proposed to adapt layer statistics to new domains \(Li et al., 2016; Chang et al., 2019\)](#). In sleep staging, a simple normalization is often applied as preprocessing, e.g., standardizing
046 signals over entire nights (Apicella et al., 2023) or short temporal windows (Chambon et al., 2018).
047 Recent studies (Gnassounou et al., 2023; 2024) highlight the importance of considering temporal
048 correlation and spectral content in normalization, proposing Temporal Monge Alignment (TMA),
049 which aligns Power Spectral Density (PSD) to a common reference using Monge mapping, going
050 beyond simple z-score normalization. However, these methods remain preprocessing steps that
cannot be inserted as layers in the network architecture as it is done with BatchNorm, LayerNorm or
InstanceNorm.
051

052 **Deep Learning for Sleep Staging** Sleep staging has been addressed by various neural network
053 architectures, which process raw signals (Chambon et al., 2018; Perslev et al., 2021; Guillot & Thorey,
2021), spectrograms (Phan et al., 2023; 2019), or both (Phan et al., 2022a). More recent approaches

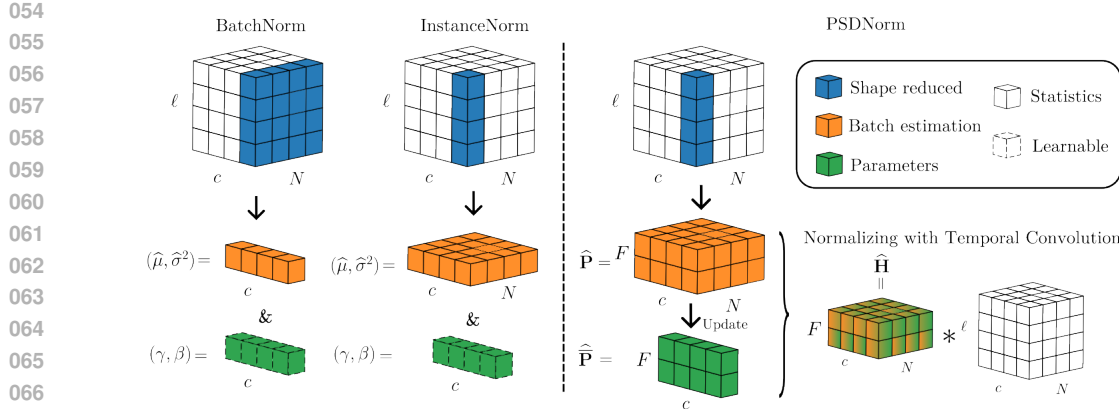


Figure 1: Description of normalization layers. The input shape is (N, c, ℓ) with batch size N , channels c , and signal length ℓ . BatchNorm estimates the mean $\hat{\mu}$ and variance $\hat{\sigma}^2$ over batch and time, and learns parameters (γ, β) to normalize the input. PSDNorm estimates PSDs $\hat{\mathbf{P}}$ over time and accounts for local temporal correlations. It computes the barycenter PSD $\hat{\mathbf{P}}$, updates it via a running Riemannian barycenter (6), and applies the filter $\hat{\mathbf{H}}$ to normalize the input. The hyperparameter f controls the extent of temporal correlation considered, thereby adjusting the strength of the normalization.

involve transformer-based models that handle multimodal (Wang et al.), spectrogram (Phan et al., 2022b), or heterogeneous inputs (Guo et al., 2024), offering improved modeling of temporal dependencies. However, most existing models are trained on relatively small cohorts, typically consisting of only a few hundred subjects, which limits their ability to generalize to diverse clinical settings. Notable exceptions include U-Sleep (Perslev et al., 2021), which was trained on a large-scale dataset and incorporates BatchNorm layers to mitigate data variability, and foundational models (Thapa et al.; Fox et al.; Deng et al.) that achieve strong generalization from vast amount of data but require significant computational resources and are challenging to adapt without fine-tuning. Our focus is on developing smaller, efficient models that balance good generalization with ease of training and deployment in clinical practice.

Contributions In this work, we introduce the PSDNorm deep learning layer, a novel approach to address distribution shifts in machine learning for signals. PSDNorm leverages Monge Mapping to incorporate temporal context and normalize feature maps effectively. This layer enhances model robustness to new subjects at inference time. Unlike standard normalization layers such as LayerNorm or InstanceNorm, PSDNorm leverages the sequential nature of intermediate feature maps, as illustrated in Figure 1. We evaluate PSDNorm through extensive experiments on 10 sleep datasets. This evaluation covers 10M of samples across 10K subjects, using a leave-one-dataset-out (LODO) protocol with 3 different random seeds. To the best of our knowledge, such a large-scale and systematic evaluation has never been conducted before. PSDNorm achieves state-of-the-art performance and requires 4 times fewer labeled data to match the accuracy of the best baseline. Results highlight the potential of PSDNorm as a practical and efficient solution for tackling domain shifts in signals.

The paper is structured as follows: Section 2 discusses existing normalization layers and pre-processing. Section 3 introduces PSDNorm, followed by numerical results in Section 4.

Notations Vectors are denoted by small cap boldface letters (e.g., \mathbf{x}), matrices by large cap boldface letters (e.g., \mathbf{X}). The element-wise product, power of n and division are denoted \odot , \odot^n and \oslash , respectively. $\llbracket 1, K \rrbracket$ denotes $\{1, \dots, K\}$. The absolute value is $| \cdot |$. The discrete circular convolution along the temporal axis operates row-wise as, $* : \mathbb{R}^{c \times \ell} \times \mathbb{R}^{c \times f} \rightarrow \mathbb{R}^{c \times \ell}$ for $\ell \geq f$. $\text{vec} : \mathbb{R}^{c \times \ell} \rightarrow \mathbb{R}^{\ell c}$ concatenates rows of a time series into a vector. $x_l = [\mathbf{x}]_l$ refers to the l^{th} element of \mathbf{x} , and $X_{l,m} = [\mathbf{X}]_{l,m}$ denotes the element of \mathbf{X} at the l^{th} row and m^{th} column. \mathbf{X}^* and \mathbf{X}^\top are the conjugate and the transpose of \mathbf{X} , respectively. diag puts the elements of a vector on the diagonal of a matrix. \otimes is the Kronecker product. $\mathbf{1}_c$ is the vector of ones of size c .

108

2 RELATED WORKS

109

110 In this section, we first review classical architectures for sleep staging and fundamental concepts of
111 normalization layers. Then, we recall the Temporal Monge Alignment (TMA) method (Gnassounou
112 et al., 2023) that aligns the PSD of signals using optimal transport.
113

114 **Deep Learning for Sleep Staging** Numerous neural network architectures have been proposed
115 for sleep staging, processing data in different formats as introduced in Section 1. Different types of
116 architectures have been explored, such as convolutional neural networks (CNNs) (Chambon et al.,
117 2018), recurrent neural networks (RNNs) (Supratak et al., 2017; Phan et al., 2019), and more recently
118 transformers (Phan et al., 2022b; Wang et al.; Guo et al., 2024), which have shown promise in
119 modeling temporal dependencies in sleep data. While many models are typically evaluated on a
120 limited number of datasets, the work by (Perslev et al., 2021) introduced U-Sleep, a model trained on
121 a large-scale dataset of sleep recordings. Their architecture, based on U-Time (Perslev et al., 2019),
122 incorporates BatchNorm layers to mitigate data variability, and they employ a domain generalization
123 approach: training a single model on a sufficiently diverse set of domains to ensure it generalizes
124 to unseen datasets without additional adaptation. This architecture is composed of encoder-decoder
125 blocks with skip connections, allowing the model to capture both local and global features of the
126 sleep signals effectively. Each encoder and decoder block consists of convolutional layers followed
127 by BatchNorm and non-linear activation functions, enabling the model to learn robust representations
128 of the input data. A more detailed description of U-Time is provided in Appendix A.3.
129

130 **Normalization Layers** Normalization layers enhance training and robustness in deep neural
131 networks. The most common are BatchNorm (Ioffe & Szegedy, 2015), InstanceNorm (Ulyanov,
132 2016), and LayerNorm (Ba et al., 2016). BatchNorm normalizes feature maps using batch and time
133 statistics, ensuring zero mean and unit variance. The output is adjusted with learnable parameters.
134 InstanceNorm normalizes each channel per sample using its own statistics, independent of the batch
135 (see Fig. 1). Popular in time-series forecasting, it is used in RevIN (Kim et al., 2021), which reverses
136 normalization after decoding. LayerNorm normalizes across all channels and time steps within each
137 sample, with learnable scaling and shifting. While these normalization layers are widely employed,
138 they operate on vectors ignoring statistical dependence and autocorrelation between their coefficients,
139 which are prevalent when operating on time-series. To address this limitation, the Temporal Monge
140 Alignment (TMA) (Gnassounou et al., 2023; 2024) was introduced as a pre-processing step to align
141 temporal correlations by leveraging the Power Spectral density (PSD) of multivariate signals using
142 Monge Optimal Transport mapping.
143

144 **Gaussian Periodic Signals** Consider a multivariate signal $\mathbf{X} \triangleq [\mathbf{x}_1, \dots, \mathbf{x}_c]^\top \in \mathbb{R}^{c \times \ell}$ of sufficient
145 length. A standard assumption is that this signal follows a centered Gaussian distribution where
146 sensors are uncorrelated and signals are periodic. This periodicity and uncorrelation structure implies
147 that the signal's covariance matrix is block diagonal, with each block having a circulant structure. A
148 fundamental property of symmetric positive definite circulant matrices is their diagonalization (Gray,
149 2006) with real and positive eigenvalues in the Fourier basis $\mathbf{F}_\ell \in \mathbb{C}^{\ell \times \ell}$ of elements
150

151
$$[\mathbf{F}_\ell]_{l,l'} \triangleq \frac{1}{\sqrt{\ell}} \exp \left(-2i\pi \frac{(l-1)(l'-1)}{\ell} \right), \quad (1)$$
152

153 where $l, l' \in \llbracket 1, \ell \rrbracket$. Hence, we have $\text{vec}(\mathbf{X}) \sim \mathcal{N}(\mathbf{0}, \Sigma)$ with Σ block-diagonal,
154

155
$$\Sigma = (\mathbf{I}_c \otimes \mathbf{F}_\ell) \text{diag}(\text{vec}(\mathbf{P})) (\mathbf{I}_c \otimes \mathbf{F}_\ell^*) \in \mathbb{R}^{c\ell \times c\ell}, \quad (2)$$
156

157 where $\mathbf{P} \in \mathbb{R}^{c \times \ell}$ contains positive entries corresponding to the Power Spectral Density of each sensor.
158 In practice, since we only have access to a single realization of the signal, the PSD is estimated with
159 only $f \ll \ell$ frequencies, i.e., $\mathbf{P} \in \mathbb{R}^{c \times f}$. This amounts to considering the local correlation of the
160 signal and neglecting the long-range correlations.
161

162 **Power Spectral Density Estimation** The Welch estimator (Welch, 1967) computes the PSD of
163 a signal by averaging the squared Fourier transform of overlapping segments of the signal. Hence,
164 the realization of the signal $\mathbf{X} \in \mathbb{R}^{c \times \ell}$ is decimated into overlapping segments $\{\mathbf{X}^{(1)}, \dots, \mathbf{X}^{(L)}\} \subset$
165

162 $\mathbb{R}^{c \times f}$ to estimate the PSD. The Welch estimator is defined as
 163

$$164 \quad \widehat{\mathbf{P}} \triangleq \frac{1}{L} \sum_{l=1}^L \left| \left((\mathbf{1}_c \mathbf{w}^\top) \odot \mathbf{X}^{(l)} \right) \mathbf{F}_f^* \right|^{\odot 2} \in \mathbb{R}^{c \times f}, \quad (3)$$

166 where $\mathbf{w} \in \mathbb{R}^f$ is the window function such that $\|\mathbf{w}\|_2 = 1$.
 167

169 **f -Monge Mapping** Let $\mathcal{N}(\mathbf{0}, \Sigma^{(s)})$ and $\mathcal{N}(\mathbf{0}, \Sigma^{(t)})$ be source and target centered Gaussian distributions respectively with covariance matrices following the structure (2) and PSDs denoted by $\mathbf{P}^{(s)}$
 170 and $\mathbf{P}^{(t)} \in \mathbb{R}^{c \times f}$. Given a signal $\mathbf{X} \in \mathbb{R}^{c \times \ell}$ such that $\text{vec}(\mathbf{X}) \sim \mathcal{N}(\mathbf{0}, \Sigma^{(s)})$, the f -Monge mapping as defined by (Gnassounou et al., 2023; 2024) is
 172

$$173 \quad m_f \left(\mathbf{X}, \mathbf{P}^{(t)} \right) \triangleq \mathbf{X} * \mathbf{H} \in \mathbb{R}^{c \times \ell}, \quad \text{where} \quad \mathbf{H} \triangleq \frac{1}{\sqrt{f}} \left(\mathbf{P}^{(t)} \oslash \mathbf{P}^{(s)} \right)^{\odot \frac{1}{2}} \mathbf{F}_f^* \in \mathbb{R}^{c \times f}. \quad (4)$$

174 In this case, f controls the alignment between the source and target distributions. Indeed, if $f = \ell$, then the f -Monge mapping is the classical Monge mapping between Gaussian distributions and the 175 source signal has its covariance matrix equal to $\Sigma^{(t)}$ after the mapping. If $f = 1$, then each sensor is only multiplied by a scalar.
 176

177 **Gaussian Wasserstein Barycenter** For Gaussian distributions admitting the decomposition (2), the 178 Wasserstein barycenter (Aguech & Carlier, 2011) admits an elegant closed-form solution. Consider 179 K centered Gaussian distributions admitting the decomposition (2) of PSDs $\mathbf{P}^{(1)}, \dots, \mathbf{P}^{(K)}$. Their 180 barycenter is also a centered Gaussian distribution $\mathcal{N}(\mathbf{0}, \bar{\Sigma})$ admitting the decomposition (2) with 181 PSD
 182

$$183 \quad \bar{\mathbf{P}} \triangleq \left(\frac{1}{K} \sum_{k=1}^K \mathbf{P}^{(k)}^{\odot \frac{1}{2}} \right)^{\odot 2} \in \mathbb{R}^{c \times f}. \quad (5)$$

184 **Temporal Monge Alignment** TMA is a pre-processing method that aligns the PSD of multi-
 185 variate signals using the f -Monge mapping. Given a source signal \mathbf{X}_s and a set of target signals
 186 $\mathbf{X}_t = \{\mathbf{X}_t^{(1)}, \dots, \mathbf{X}_t^{(K)}\}$, the TMA method uses the f -Monge mapping between the source and the
 187 Wasserstein barycenter of the target signals. Hence, it simply consists of 1) estimating the PSD of
 188 all the signals, 2) computing the Wasserstein barycenter of the target signals, and 3) applying the
 189 f -Monge mapping to the source signal. TMA, as a preprocessing method, is inherently limited to
 190 handling PSD shifts in the raw signals and cannot address more complex distributional changes in the
 191 data. This limitation highlights the need for a layer that can effectively capture and adapt to these
 192 complex variations during learning and inside deep learning models.
 193

194 3 PSDNORM LAYER

195 The classical normalization layers, such as BatchNorm or InstanceNorm do not take into account
 196 the temporal autocorrelation structure of signals. They treat each time sample in the intermediate
 197 representations independently. In this section, we introduce the PSDNorm layer that aligns the PSD
 198 of each signal onto a barycenter PSD within the architecture of a deep learning model.
 199

200 PSDNorm is a novel normalization layer that can be used as a drop-in replacement for layers
 201 like BatchNorm or InstanceNorm. Instead of simple standardization, it aligns the Power Spectral
 202 Density (PSD) of feature maps to a running barycenter PSD. This approach, optimized for modern
 203 hardware, enhances model robustness to new subjects at inference time without retraining. We
 204 define the normalized feature map as $\tilde{\mathbf{G}} \triangleq \text{PSDNorm}(\mathbf{G})$. The following sections introduce the core
 205 components of PSDNorm and its implementation.
 206

207 3.1 CORE COMPONENTS OF THE LAYER

208 In the following, we formally define PSDNorm and present each of its three main components: 1) PSD
 209 estimation, 2) running Riemannian barycenter estimation, and 3) f -Monge mapping computation.
 210 Given a batch $\mathcal{B} = \{\mathbf{G}^{(1)}, \dots, \mathbf{G}^{(N)}\}$ of N pre-normalization feature maps, PSDNorm outputs a
 211

normalized batch $\tilde{\mathcal{B}} = \{\tilde{\mathbf{G}}^{(1)}, \dots, \tilde{\mathbf{G}}^{(N)}\}$ with normalized PSD. Those three steps are detailed in the following and illustrated in the right part of Figure 1.

PSD Estimation First, the estimation of the PSD of each feature map is performed using the Welch method. The per-channel mean $\hat{\mu}^{(j)}$ is computed for each feature map $\mathbf{G}^{(j)}$ as $\hat{\mu}^{(j)} \triangleq \frac{1}{\ell} \sum_{l=1}^{\ell} [\mathbf{G}^{(j)}]_{:,l} \in \mathbb{R}^c$.

Then, the PSD of the centered feature map $\mathbf{G}^{(j)} - \hat{\mu}^{(j)} \mathbf{1}_{\ell}^{\top}$, denoted $\hat{\mathbf{P}}^{(j)}$, is estimated as described in Equation (3). This centering step is required as feature maps are typically non-centered due to activation functions and convolution biases but they are assumed to have a stationary mean. The Welch estimation involves segmenting the centered feature map into overlapping windows, computing the Fourier transform of each window and then averaging them.

Geodesic and Running Riemanian Barycenter The PSDNorm aligns the PSD of each feature map to a barycenter PSD. This barycenter is computed during training by interpolating between the batch Wasserstein barycenter and the current running Riemanian barycenter using the geodesic associated with the Bures metric (Bhatia et al., 2019). The batch barycenter is first computed from the current batch PSDs $\{\hat{\mathbf{P}}^{(1)}, \dots, \hat{\mathbf{P}}^{(N)}\}$ using Equation (5). To ensure gradual adaptation, the running barycenter is updated via an exponential geodesic average with $\alpha \in [0, 1]$:

$$\hat{\mathbf{P}} \leftarrow \left((1 - \alpha) \hat{\mathbf{P}}^{\odot \frac{1}{2}} + \alpha \hat{\mathbf{P}}_B^{\odot \frac{1}{2}} \right)^{\odot 2} \in \mathbb{R}^{c \times f}. \quad (6)$$

A proof of the geodesic is provided in Appendix A.1.

PSD Adaptation with f -Monge Mapping The final step of the PSDNorm is the application of the f -Monge mapping to each feature map after subtracting the per-channel mean. Indeed, for all $j \in \llbracket 1, N \rrbracket$, it is defined as

$$\tilde{\mathbf{G}}^{(j)} = m_f \left(\mathbf{G}^{(j)} - \hat{\mu}^{(j)} \mathbf{1}_{\ell}^{\top}, \hat{\mathbf{P}} \right) = \left(\left(\mathbf{G}^{(j)} - \hat{\mu}^{(j)} \mathbf{1}_{\ell}^{\top} \right) * \hat{\mathbf{H}}^{(j)} \right) \in \mathbb{R}^{c \times \ell} \quad (7)$$

where $\hat{\mathbf{H}}^{(j)}$ is the Monge mapping filter computed as

$$\hat{\mathbf{H}}^{(j)} \triangleq \frac{1}{\sqrt{f}} \left(\hat{\mathbf{P}} \oslash \hat{\mathbf{P}}^{(j)} \right)^{\odot \frac{1}{2}} \mathbf{F}_f^* \in \mathbb{R}^{c \times f} \quad (8)$$

where $\hat{\mathbf{P}}^{(j)}$ is the estimated PSD of $\mathbf{G}^{(j)} - \hat{\mu}^{(j)} \mathbf{1}_{\ell}^{\top}$.

3.2 IMPLEMENTATION DETAILS

Overall Algorithm The forward computation of the proposed layer is outlined in Algorithm 1. At train time, the PSDNorm performs three main operations: 1) PSD estimation, 2) running Riemannian barycenter update, and 3) Monge mapping application. At inference, the PSDNorm operates similarly, except it does not update the running barycenter. The PSDNorm is fully differentiable and can be integrated into any deep learning model. Similarly to classical normalization layers, a stop gradient operation is applied to the running barycenter to prevent the backpropagation of the gradient computation through the barycenter. PSDNorm has a unique additional hyperparameter f which is the filter size. It controls the alignment between each feature map and the running barycenter PSD and it is typically chosen in our experiments between 1 and 17. In practice, the Fourier transforms are efficiently computed using the Fast Fourier Transform (FFT) algorithm. Because of the estimation of PSDs, the complexity of the PSDNorm, both at train and inference times, is $\mathcal{O}(N c \ell f \log(f))$, where N is the batch size, c the number of channels, ℓ the signal length, and f the filter size.

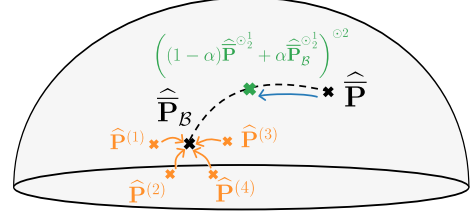


Figure 2: **Description of the running Riemanian barycenter.** The barycenter of the batch $\hat{\mathbf{P}}_B$ is estimated from the PSD of each batch sample.

270 3.3 DISCUSSION AND CONNECTIONS TO RELATED METHODS
271

272 **PSDNorm as a generalization of InstanceNorm** InstanceNorm applies
273 a per-channel z -score over time, subtracting the mean and dividing by
274 the standard deviation—equivalent to whitening under an i.i.d. assumption
275 over time. In contrast, PSDNorm explicitly accounts for temporal
276 structure by estimating the PSD and whitening/re-coloring in the
277 frequency domain. InstanceNorm is recovered as a special case of PSDNorm
278 by setting the filter size to $f = 1$ and using the uniform PSD barycenter as
279 $\hat{\mathbf{P}} = \mathbf{1}$. as the re-coloring transform
280 instead of the barycentric PSD.
281
282
283
284
285
286
287
288
289
290

291 **Similarity with Test-time Domain Adaptation** PSDNorm is inspired by Temporal Monge Alignment
292 (TMA) (Gnassounou et al., 2023), a pre-processing technique that can be used for test-time
293 adaptation. Test-time Domain Adaptation methods adjust a pre-trained model to a new target domain
294 during inference, without requiring access to the original training data (Wang et al., 2021; Yang et al.,
295 2021). While PSDNorm must be integrated into the model during training and is not a post-hoc
296 adaptation method, it provides a similar benefit at inference time. Designing new modern architectures
297 that incorporate PSDNorm can enhance robustness to domain shifts without the need for retraining or
298 access to source data.
299

300 **Discussion of Gaussian and Stationarity Assumptions** PSDNorm relies on the Gaussian ap-
301 proximation of OT for compensation variability but does not assume that the signals are Gaussian.
302 This allows for efficient alignment of second-order statistics (covariance structure), but also allows
303 preserving higher-order discriminative information. This approach is computationally tractable and
304 targets the most prominent sources of domain shift without over-distorting the signal, a strategy also
305 used in successful methods like Deep CORAL (Sun & Saenko, 2016). Like BatchNorm, PSDNorm
306 assumes shifts are captured by low-order statistics, but it provides a richer alignment by incorporating
307 temporal context.
308

309 4 NUMERICAL EXPERIMENTS
310

311 In this section, we evaluate the proposed method
312 through a series of experiments designed to high-
313 light its effectiveness and robustness on the clin-
314 ically relevant task of sleep staging. We first de-
315 scribe the datasets and training setup employed,
316 followed by a performance comparison with ex-
317 isting normalization techniques. Next, we as-
318 sess the efficiency of PSDNorm by training over
319 varying numbers of subjects per dataset. Finally,
320 we analyze the robustness of PSDNorm against
321 domain shift by focusing on subject-wise per-
322 formance and different architectures. The code
323 will be available on GitHub upon acceptance. The anonymized code is available in the supplementary
material. All numerical experiments were conducted using a total of 1500 GPU hours on NVIDIA
H100 GPUs.
324

Algorithm 1 Forward pass of PSDNorm

```

1: Input: Batch  $\mathcal{B} = \{\mathbf{G}^{(1)}, \dots, \mathbf{G}^{(N)}\}$ , running
   barycenter  $\hat{\mathbf{P}}$ , filter-size  $f$ , momentum  $\alpha$ , training flag
2: Output: Normalized batch  $\{\tilde{\mathbf{G}}^{(1)}, \dots, \tilde{\mathbf{G}}^{(N)}\}$ 
3: for  $j = 1$  to  $N$  do
4:    $\hat{\boldsymbol{\mu}}^{(j)} \leftarrow$  Mean estimation
5:    $\hat{\mathbf{P}}^{(j)} \leftarrow$  PSD est. from  $\tilde{\mathbf{G}}^{(j)} - \hat{\boldsymbol{\mu}}^{(j)} \mathbf{1}_\ell^\top$  with eq. (3)
6: end for
7: if training then
8:    $\hat{\mathbf{P}}_{\mathcal{B}} \leftarrow$  Batch bary. from  $\{\hat{\mathbf{P}}^{(j)}\}_j$  with eq. (5)
9:    $\hat{\mathbf{P}} \leftarrow$  Running bary. up. from  $\hat{\mathbf{P}}, \hat{\mathbf{P}}_{\mathcal{B}}$  with eq. (6)
10: end if
11: for  $j = 1$  to  $N$  do
12:    $\hat{\mathbf{H}}^{(j)} \leftarrow$  Filter estimation from  $\hat{\mathbf{P}}^{(j)}, \hat{\mathbf{P}}$  with eq. (8)
13:    $\tilde{\mathbf{G}}^{(j)} \leftarrow f$ -Monge mapping with eq. (7)
14: end for

```

Table 1: Characteristics of the datasets.

Dataset	Subj.	Rec.	Age \pm std	Sex (F/M)
ABC	44	117	48.8 ± 9.8	43%/57%
CCSHS	515	515	17.7 ± 0.4	50%/50%
CFS	681	681	41.7 ± 20.0	55%/45%
HPAP	166	166	46.5 ± 11.9	43%/57%
MROS	2101	2698	76.4 ± 5.5	0%/100%
PHYS	70	132	58.8 ± 22.0	33%/67%
SHHS	5730	8271	63.1 ± 11.2	52%/48%
MASS	61	61	42.5 ± 18.9	55%/45%
CHAT	1230	1635	6.6 ± 1.4	52%/48%
SOF	434	434	82.8 ± 3.1	100%/0%
Total	11032	14710	—	—

324
325

4.1 EXPERIMENTAL SETUP

326
327
328
329
330
331
332
333
334
335

Datasets To evaluate the effect of normalization layers, we use ten datasets of sleep staging described in Table 1. ABC (Jessie P. et al., 2018), CCSHS (Rosen et al., 2003), CFS (Redline et al., 1995), HPAP (Rosen et al., 2012), MROS (Blackwell et al., 2011), SHHS (Quan et al., 1998), CHAT (Marcus et al., 2013), and SOF (Spira et al., 2008) are publicly available sleep datasets with restricted access from National Sleep Research Resource (NSRR) (Zhang et al., 2018). PHYS (Goldberger et al., 2000) and MASS (O'Reilly et al., 2014) are two other datasets publicly available. Every 30 s epoch is labeled with one of the five sleep stages: Wake, N1, N2, N3, and REM. These datasets are unbalanced in terms of age, sex, number of subjects, and have been recorded with different sensors in different institutions which makes the sleep staging task challenging. We now describe the pre-processing steps and splits of the datasets.

336
337
338
339
340
341
342
343

Data Pre-processing We follow a standard pre-processing pipeline used in the field (Chambon et al., 2017; Stephansen et al., 2018). The datasets vary in the number and type of available EEG and electrooculogram (EOG) channels. To ensure consistency, we use two bipolar EEG channels, as some datasets lack additional channels. For dataset from NSRR, we select the channels C3-A2 and C4-A1. For signals from Physionet and MASS, we use the only available channels Fpz-Cz and Pz-Oz. The EEG signals are low-pass filtered with a 30 Hz cutoff frequency and resampled to 100 Hz. All data extraction and pre-processing steps are implemented using MNE-BIDS (Appelhoff et al., 2019) and MNE-Python (Gramfort et al., 2013).

344
345
346
347
348
349
350
351
352

Leave-One-Dataset-Out (LODO) Setup and Balancing We evaluate model performance using a leave-one-dataset-out (LODO) protocol: in each fold, one dataset is held out for testing, and the model is trained on the union of the remaining datasets. From the training data, 80% of subjects are used for training and 20% for validation, which is used for early stopping. The full held-out dataset is used for testing. To assess performance in low-data regimes, we also evaluate a variant in which we subsample at most N subjects per dataset, promoting balanced contributions across training sources. We refer to this configuration as **balanced@ N** , with N ranging from 40 to 400. The exact number of subjects per dataset in each case is listed in Appendix Table 3.

353
354
355
356
357
358
359
360
361
362

Architecture and Training Sleep staging has inspired a variety of neural architectures, from early CNN-based models (Chambon et al., 2017; Stephansen et al., 2018; Phan et al., 2022a) to recent attention-based approaches (Phan et al., 2022b; 2023; Wang et al.). We evaluate two architectures: **U-Sleep** (Perslev et al., 2019; 2021), a state-of-the-art temporal CNN model designed for robustness and large-scale training, and a newly introduced architecture, **CNNTransformer**. CNNTransformer combines a lightweight convolutional encoder with a Transformer applied to epoch-level embeddings. It is specifically tailored for two-channel EEG and designed to scale efficiently to large datasets, while remaining minimal in implementation (under 100 lines of code) and training cost (Appendix A.4). Its design draws inspiration from recent transformer-based models for time series (Yang et al., 2023), with an emphasis on simplicity and practicality.

363
364
365
366
367
368
369

We use the Adam optimizer (Kingma, 2014) with a learning rate of 10^{-3} to minimize the weighted cross-entropy loss, where class weights are computed from the training set distribution. Training is performed with a batch size of 64, and early stopping is applied based on validation loss with a patience of 3 epochs. Each input corresponds to a sequence of 17'30s, with a stride of 10'30s between sequences along the full-night recording. The filter size f of PSDNorm is set to 5. A sensitivity analysis of f is provided in Appendix A.6 in the appendix, and show that the performance is stable across a range of values from 5 to 11.

370
371
372
373
374

Evaluation At inference, the model similarly processes sequences of 17'30s with a stride of 10'30s. Performance is evaluated using the balanced accuracy score (BACC), computed on the central 10'30s of each prediction window. Each experiment is repeated three times with different random seeds, and we report the mean and standard deviation of BACC.

375
376
377

Normalization Strategies We compare the proposed PSDNorm with three normalization strategies: BatchNorm, LayerNorm, and InstanceNorm. Note that InstanceNorm corresponds to a special case of PSDNorm with $f = 1$ and a fixed identity mapping instead of a learned running barycenter. In the following experiments, the BatchNorm layers in the first three convolutional layers are replaced

378
 379
 380
 381
 382
 383
 384 Table 2: **Balanced Accuracy (BACC) scores on the left-out datasets with USleep.** The top
 385 section reports results in the **large-scale** setting (using all available subjects), while the bottom
 386 section presents results in the **medium-scale** setting (balanced@400). For each row, the best score is
 387 highlighted in **bold**, and standard deviations reflect training variability across 3 random seeds. The
 388 mean BACC reports the average over all the subjects.
 389
 390
 391
 392
 393
 394
 395
 396
 397
 398
 399
 400
 401
 402
 403
 404
 405
 406
 407
 408

	Dataset	BatchNorm	LayerNorm	InstanceNorm	TMA	PSDNorm
All subjects	ABC	78.49 \pm 0.42	77.94 \pm 0.31	78.83\pm0.59	78.33 \pm 0.12	78.56 \pm 0.67
	CCSHS	88.79\pm0.21	87.51 \pm 0.77	88.75 \pm 0.04	88.61 \pm 0.10	88.56 \pm 0.36
	CFS	84.97 \pm 0.37	84.29 \pm 0.67	85.73\pm0.29	84.85 \pm 0.13	85.42 \pm 0.09
	CHAT	64.72 \pm 3.94	64.36 \pm 0.40	68.86 \pm 2.49	69.76 \pm 1.62	70.57\pm1.24
	HOMEPA	76.39 \pm 0.29	75.23 \pm 0.78	76.70 \pm 0.35	76.77\pm0.66	76.72 \pm 0.27
	MASS	73.71 \pm 0.62	71.39 \pm 3.00	72.12 \pm 0.70	73.90\pm0.69	72.51 \pm 1.68
	MROS	81.30 \pm 0.25	80.44 \pm 0.29	81.49 \pm 0.18	80.91 \pm 0.42	81.57\pm0.34
	PhysioNet	76.13 \pm 0.57	75.12 \pm 0.22	76.15 \pm 0.52	76.48\pm0.37	75.96 \pm 1.02
	SHHS	77.97 \pm 1.46	75.98 \pm 0.48	79.05 \pm 0.89	78.21 \pm 0.39	79.14\pm1.01
	SOF	81.33 \pm 0.54	81.82 \pm 0.79	81.98 \pm 0.22	81.84 \pm 0.49	82.50\pm0.34
Balanced@400	Mean(Dataset)	78.38 \pm 0.47	77.41 \pm 0.28	78.97 \pm 0.11	78.98 \pm 0.14	79.15\pm0.14
	Mean(Subject)	78.14 \pm 1.01	76.78 \pm 0.18	79.26 \pm 0.48	78.77 \pm 0.07	79.51\pm0.62
	ABC	78.26 \pm 1.33	75.29 \pm 0.81	78.73\pm0.42	78.04 \pm 0.51	78.18 \pm 0.68
	CCSHS	87.42 \pm 0.16	85.20 \pm 0.48	87.62\pm0.42	87.57 \pm 0.20	87.58 \pm 0.30
	CFS	84.32 \pm 0.57	81.66 \pm 1.36	84.72\pm0.33	84.58 \pm 0.20	84.29 \pm 0.36
	CHAT	66.55 \pm 0.88	61.19 \pm 1.16	64.43 \pm 4.41	68.73 \pm 2.48	70.28\pm1.70
	HOMEPA	75.25 \pm 0.50	74.86 \pm 0.25	76.47\pm0.63	76.10 \pm 0.32	76.83\pm0.61
	MASS	70.00 \pm 1.91	68.56 \pm 3.33	71.52 \pm 1.13	71.63 \pm 1.92	72.77\pm1.09
	MROS	80.37\pm0.20	78.05 \pm 0.22	80.28 \pm 0.21	80.09 \pm 0.40	80.26 \pm 0.11
	PhysioNet	75.81\pm0.13	71.82 \pm 2.12	74.68 \pm 0.55	75.31 \pm 1.54	74.82 \pm 2.11
405	SHHS	76.44 \pm 0.92	75.12 \pm 0.39	78.68 \pm 0.37	77.00 \pm 0.39	78.88\pm0.68
	SOF	81.08 \pm 1.14	78.70 \pm 0.50	80.68 \pm 1.38	81.25\pm0.71	79.49 \pm 0.41
406	Mean(Dataset)	77.55 \pm 0.34	75.05 \pm 0.28	77.78 \pm 0.46	78.03 \pm 0.35	78.34\pm0.42
	Mean(Subject)	77.22 \pm 0.34	75.04 \pm 0.42	78.17 \pm 0.28	77.74 \pm 0.36	78.85\pm0.59

407
 408
 409 with either PyTorch’s default implementations of LayerNorm, InstanceNorm (Paszke et al., 2019), or
 410 PSDNorm. To preserve the receptive field, the filter size f of PSDNorm is used in the first layer and
 411 progressively halved in the following ones. We fix the momentum α to 10^{-2} .
 412

413 4.2 NUMERICAL RESULTS

414
 415 This section presents results from large-scale sleep stage classification experiments. The analysis be-
 416 gins with a comparison of PSDNorm against standard normalization layers—BatchNorm, LayerNorm,
 417 and InstanceNorm—on the full datasets. Then, the data efficiency of each method is evaluated under
 418 limited training data regimes. Finally, robustness to distribution shift is assessed via subject-wise
 419 performance across multiple neural network architectures.
 420

421 **Performance Comparison on Full Datasets** Table 2 (top) reports the LODO BACC of U-Sleep
 422 across all datasets, averaged over three random seeds. PSDNorm consistently outperforms all
 423 baseline normalization layers—BatchNorm, LayerNorm, InstanceNorm, and TMA—achieving the
 424 highest mean BACC of 79.51% over subjects, which exceeds BatchNorm (78.38%), InstanceNorm
 425 (78.97%), LayerNorm (77.41%) and TMA (78.77%). On the challenging CHAT dataset, where all
 426 methods struggle, PSDNorm outperforms all other normalizations by more than 1 percentage points,
 427 highlighting its robustness under strong distribution shifts. Although InstanceNorm is a strong base-
 428 line—outperforming BatchNorm and LayerNorm by at least one standard deviation on average—it is
 429 consistently surpassed by PSDNorm in average performance. In contrast, LayerNorm underperforms
 430 across the board, achieving the lowest average BACC and never ranking first, confirming its limited
 431 suitability for this task. PSDNorm also improves score by almost 1% over TMA, showing that using
 432 Monge Alignment inside the network allows for better adaptation.
 433

432
Efficiency: Performance with 4× Less Data
433 The PSDNorm layer improves model per-
434 formance when trained on the full dataset
435 (~ 10000 subjects), but such large-scale data
436 availability is not always the case. In many
437 real-world scenarios—such as rare disease
438 studies, pediatric populations, or data col-
439 lected in constrained clinical settings—labeled
440 recordings are scarce, expensive to annotate,
441 or restricted due to privacy concerns. Evaluat-
442 ing model robustness under these constraints
443 is therefore essential. To this end, we train all
444 models using the balanced@400 setup, which
445 reduces the training data by a factor of 4 com-
446 pared to the full-data setting. In this lower-
447 data regime, PSDNorm continues to outperform all
448 baseline normalization strategies and achieves
449 higher average BACC. The performance improve-
450 ment of PSDNorm over the best baseline is more
451 pronounced in this setting: the BACC gain reaches
452 $+0.67\%$, compared to $+0.25\%$ in the full-data
453 setting. The gains exceed one standard devia-
454 tion. To assess statistical significance, we con-
455 ducted a critical difference (CD) test (Demšar,
456 2006). Figure 3 (top) reports the average rank
457 of each method and the corresponding statis-
458 tical comparisons. The results confirm that PSDNorm
459 significantly out-
460 performs the baselines, underscoring the value of incor-
461 porating temporal structure into normalization
462 for robust and data-efficient generalization.
463 The same trend is observed for U-Sleep trained on all
464 subjects (see in Appendix Figure 8). The following experiments focus on the balanced@400 setup.

465
Robustness Across Architectures PSDNorm is a plug-and-play normalization layer that can be
466 seamlessly integrated into various neural network architectures. To demonstrate this flexibility, we
467 evaluate its performance on both the U-Sleep and CNNTransformer models. Figure 3 reports the
468 average rank of each normalization method across datasets and subjects for both architectures using
469 datasets balanced@400. In both architectures, PSDNorm achieves the best overall ranking and
470 demonstrates statistically significant improvements over both BatchNorm, InstanceNorm, and TMA.
471 The results confirm that PSDNorm generalizes well beyond a single architecture and can provide
472 consistent improvements in diverse modeling setups which is not the case of TMA that is ranked
473 the worst with CNNTransformer. InstanceNorm performs competitively in some cases but is never
474 significantly better than PSDNorm. Detailed numerical scores for CNNTransformer are reported in
475 the supplementary material (Table 7).

476 It is important to highlight that PSDNorm brings improvements without too much additional compu-
477 tational cost. In appendix Appendix A.12 we provide a detailed comparison of the computational
478 time of PSDNorm with other normalization layers. The results show that PSDNorm is only slightly
479 slower than BatchNorm and InstanceNorm, with a negligible increase in training time (less than 10%)
480 and no significant impact on inference speed.

481
Performance on the most challenging subjects
482 Performance variability across subjects is a key
483 challenge in biomedical applications where en-
484 suring consistently high performance—even for
485 the most challenging subjects—is critical. To
486 highlight the robustness of PSDNorm, Figure 4
487 presents a scatter plot of subject-wise BACC
488 scores comparing BatchNorm or InstanceNorm
489 vs. PSDNorm across two selected target datasets.
490 CHAT and MASS are two challenging datasets,
491 where the prediction performance is significantly
492 lower than the other datasets. For CHAT, most of
493 the dots are below the diagonal, indicating that PS-
494 DNorm improves performance for 91% of subjects
495 against BatchNorm and 99% of subjects against
496 InstanceNorm, with the largest gains observed for

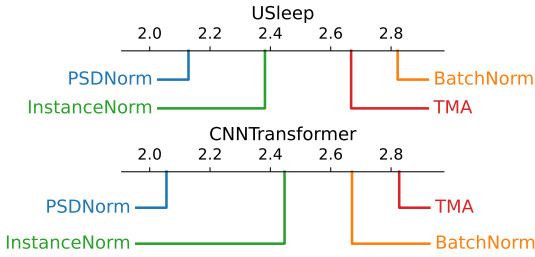


Figure 3: **Critical Difference (CD) diagram for two architectures on datasets balanced @400.** Average ranks across datasets and subjects for USleep and CNNTransformer. Black lines connect methods that are not significantly different.

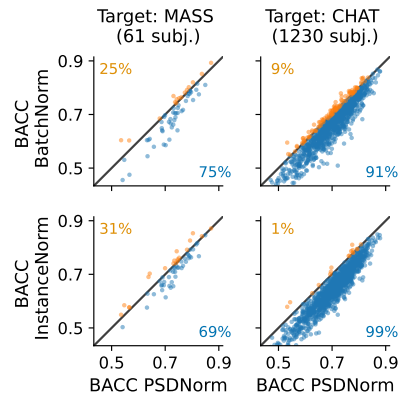


Figure 4: **Subject-wise BACC comparison on MASS and CHAT (balanced @400).** Blue dot means improvement with PSDNorm.

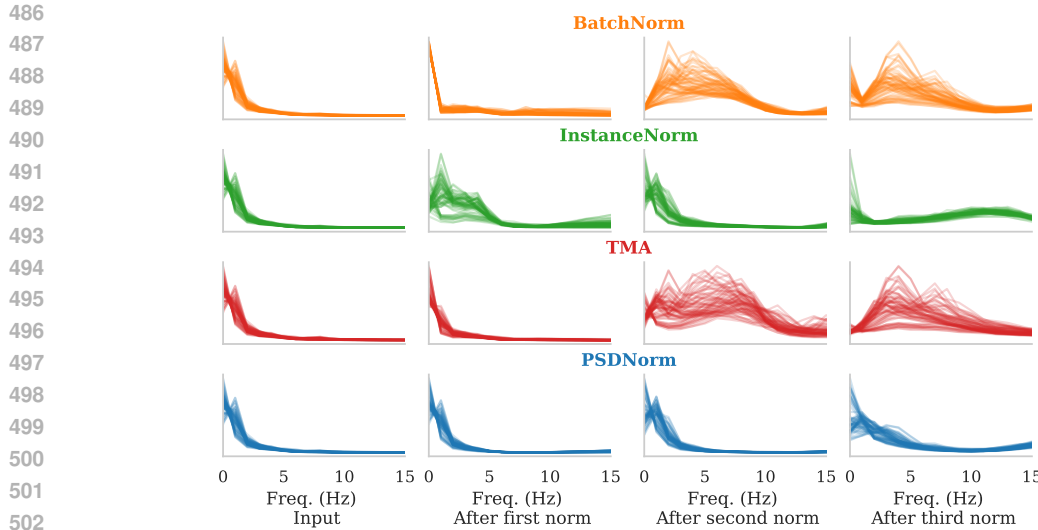


Figure 5: **Illustration of PSD normalization with different normalization layers.** The figure shows the PSD of different segment of 17min from one subject batch as input, and after 3 encoders using different normalization layers.

the hardest subjects, reinforcing its ability to handle challenging cases. For MASS, PSDNorm improves performance for 75% of subjects against BatchNorm and 69% against InstanceNorm. This demonstrates that PSDNorm is not only effective in improving overall performance but also excels in enhancing the performance of the most challenging subjects.

4.3 ILLUSTRATION OF PSD NORMALIZATION

Figure 5 shows how different normalization layers affect the PSD of signals at several stages of the network. The input signals display limited variability, which explains why applying TMA as a pre-processing step provides only marginal benefit. In the first row, corresponding to BatchNorm, the PSD variability increases with depth, a behavior that is undesirable for generalization. TMA exhibits a similar pattern, as no normalization is applied within the network to counteract this accumulation of variance. In contrast, both InstanceNorm and PSDNorm reduce PSD variability across samples. However, InstanceNorm does not fully align the PSDs, and noticeable differences remain between samples. PSDNorm, on the other hand, achieves strong alignment of PSDs across samples, indicating its ability to normalize the underlying temporal correlations. In addition, PSDNorm gives more consistent PSDs across different layers of the network giving a better stability compare to InstanceNorm. This alignment is essential for improving robustness and generalization, particularly in settings involving distribution shifts.

5 CONCLUSION, LIMITATIONS, AND FUTURE WORK

This paper introduced PSDNorm, a normalization layer that aligns the power spectral density (PSD) of each signal to a geodesic barycenter. By leveraging temporal correlations, PSDNorm offers a principled alternative to standard normalization layers. Experiments on large-scale sleep staging datasets show that PSDNorm consistently improves performance, robustness, and data efficiency, especially under domain shift and limited-data settings—outperforming BatchNorm, LayerNorm, and InstanceNorm across architectures.

While the results are promising, some limitations remain. PSDNorm introduces a filter size hyperparameter (f) that controls normalization strength; although we provide default values that perform well across datasets, selecting it automatically in adaptive settings could be challenging.

Despite these limitations, PSDNorm is flexible and easy to integrate into existing models. Future work includes extending it to other signals such as audio and other biomedical applications.

540 REFERENCES
541

542 Martial Agueh and Guillaume Carlier. Barycenters in the wasserstein space. *SIAM Journal on*
543 *Mathematical Analysis*, 43(2):904–924, 2011.

544 Andrea Apicella, Francesco Isgrò, Andrea Pollastro, and Roberto Prevete. On the effects of data nor-
545 malization for domain adaptation on EEG data. *Engineering Applications of Artificial Intelligence*,
546 123:106205, 2023.

547 Stefan Appelhoff, Matthew Sanderson, Teon L. Brooks, Marijn van Vliet, Romain Quentin, Chris
548 Holdgraf, Maximilien Chaumon, Ezequiel Mikulan, Kambiz Tavabi, Richard Höchenberger,
549 Dominik Welke, Clemens Brunner, Alexander P. Rockhill, Eric Larson, Alexandre Gramfort,
550 and Mainak Jas. MNE-BIDS: Organizing electrophysiological data into the BIDS format and
551 facilitating their analysis. *Journal of Open Source Software*, 4(44):1896, 2019. doi: 10.21105/joss.
552 01896.

553 Jimmy Lei Ba, Jamie Ryan Kiros, and Geoffrey E. Hinton. Layer normalization, 2016. URL
554 <http://arxiv.org/abs/1607.06450>.

555 Rajendra Bhatia, Tanvi Jain, and Yongdo Lim. On the bures–wasserstein distance between positive
556 definite matrices. *Expositiones Mathematicae*, 37(2):165–191, 2019.

557 Terri Blackwell, Kristine Yaffe, Sonia Ancoli-Israel, Susan Redline, Kristine E. Ensrud, Marcia L. Stefanick, Alison Laffan, Katie L. Stone, and Osteoporotic Fractures in Men Study
558 Group. Associations between sleep architecture and sleep-disordered breathing and cognition
559 in older community-dwelling men: the Osteoporotic Fractures in Men Sleep Study. *Journal of*
560 *the American Geriatrics Society*, 59(12):2217–2225, December 2011. ISSN 1532-5415. doi:
561 10.1111/j.1532-5415.2011.03731.x.

562 Stanislas Chambon, Mathieu Galtier, Pierrick Arnal, Gilles Wainrib, and Alexandre Gramfort. A
563 deep learning architecture for temporal sleep stage classification using multivariate and multimodal
564 time series. 2017.

565 Stanislas Chambon, Mathieu N Galtier, Pierrick J Arnal, Gilles Wainrib, and Alexandre Gramfort. A
566 deep learning architecture for temporal sleep stage classification using multivariate and multimodal
567 time series. *IEEE Transactions on Neural Systems and Rehabilitation Engineering*, 26(4):758–769,
568 2018.

569 Woong-Gi Chang, Tackgeun You, Seonguk Seo, Suha Kwak, and Bohyung Han. Domain-specific
570 batch normalization for unsupervised domain adaptation, 2019. URL <https://arxiv.org/abs/1906.03950>.

571 Janez Demšar. Statistical comparisons of classifiers over multiple data sets. *Journal of Machine*
572 *Learning Research*, 7(1):1–30, 2006. URL <http://jmlr.org/papers/v7/demsar06a.html>.

573 Guifeng Deng, Mengfan Niu, Yuxi Luo, Shuying Rao, Junyi Xie, Zhenghe Yu, Wenjuan Liu, Sha
574 Zhao, Gang Pan, Xiaojing Li, Wei Deng, Wanjun Guo, Tao Li, and Haiteng Jiang. A unified
575 flexible large polysomnography model for sleep staging and mental disorder diagnosis. pp.
576 2024.12.11.24318815. doi: 10.1101/2024.12.11.24318815. URL <https://www.ncbi.nlm.nih.gov/pmc/articles/PMC11661386/>.

577 Benjamin Fox, Joy Jiang, Sajila Wickramaratne, Patricia Kovatch, Mayte Suarez-Farinas, Neomi A.
578 Shah, Ankit Parekh, and Girish N. Nadkarni. A foundational transformer leveraging full night,
579 multichannel sleep study data accurately classifies sleep stages. pp. zsaf061. ISSN 1550-9109.
580 doi: 10.1093/sleep/zsaf061.

581 Théo Gnassounou, Antoine Collas, Rémi Flamary, Karim Lounici, and Alexandre Gramfort. Multi-
582 source and test-time domain adaptation on multivariate signals using spatio-temporal monge
583 alignment. *arXiv preprint arXiv:2407.14303*, 2024.

584 Théo Gnassounou, Rémi Flamary, and Alexandre Gramfort. Convolutional monge mapping nor-
585 malization for learning on biosignals. In *Neural Information Processing Systems (NeurIPS)*,
586 2023.

594 Ary Goldberger, Luís Amaral, L. Glass, Shlomo Haylin, J. Hausdorg, Plamen Ivanov, R. Mark,
 595 J. Mietus, G. Moody, Chung-Kang Peng, H. Stanley, and Physiotoolkit Physiobank. Components
 596 of a new research resource for complex physiologic signals. *PhysioNet*, 101, 01 2000.

597

598 Alexandre Gramfort, Martin Luessi, Eric Larson, Denis A. Engemann, Daniel Strohmeier, Christian
 599 Brodbeck, Roman Goj, Mainak Jas, Teon Brooks, Lauri Parkkonen, and Matti S. Hämäläinen.
 600 MEG and EEG data analysis with MNE-Python. *Frontiers in Neuroscience*, 7(267):1–13, 2013.
 601 doi: 10.3389/fnins.2013.00267.

602 Robert M. Gray. Toeplitz and circulant matrices: A review. *Foundations and Trends® in Communica-
 603 tions and Information Theory*, 2(3):155–239, 2006. ISSN 1567-2190. doi: 10.1561/0100000006.
 604 URL <http://dx.doi.org/10.1561/0100000006>.

605

606 Antoine Guillot and Valentin Thorey. RobustSleepNet: Transfer learning for automated sleep staging
 607 at scale. 2021.

608 Yanchen Guo, Maciej Nowakowski, and Weiying Dai. Flexsleeptransformer: a transformer-based
 609 sleep staging model with flexible input channel configurations. *Scientific Reports*, 14, 11 2024.
 610 doi: 10.1038/s41598-024-76197-0.

611

612 Sergey Ioffe and Christian Szegedy. Batch normalization: accelerating deep network training
 613 by reducing internal covariate shift. In *Proceedings of the 32nd International Conference on
 614 International Conference on Machine Learning - Volume 37*, ICML’15, pp. 448–456. JMLR.org,
 2015.

615

616 Bakker Jessie P., Tavakkoli Ali, Rueschman Michael, Wang Wei, Andrews Robert, Malhotra
 617 Atul, Owens Robert L., Anand Amit, Dudley Katherine, and Patel Sanya R. Gastric Band-
 618 ing Surgery versus Continuous Positive Airway Pressure for Obstructive Sleep Apnea: A
 619 Randomized Controlled Trial. *American journal of respiratory and critical care medicine*,
 620 197(8), April 2018. ISSN 1535-4970. doi: 10.1164/rccm.201708-1637LE. URL <https://pubmed.ncbi.nlm.nih.gov/29035093/>. Publisher: Am J Respir Crit Care Med.

621

622 Taesung Kim, Jinhee Kim, Yunwon Tae, Cheonbok Park, Jang-Ho Choi, and Jaegul Choo. Re-
 623 versible instance normalization for accurate time-series forecasting against distribution shift. In
 624 *International Conference on Learning Representations*, 2021.

625

626 Diederik P Kingma. Adam: A method for stochastic optimization. *arXiv preprint arXiv:1412.6980*,
 627 2014.

628

629 Reinmar Kobler, Jun-ichiro Hirayama, Qibin Zhao, and Motoaki Kawanabe. Spd domain-specific
 630 batch normalization to crack interpretable unsupervised domain adaptation in EEG. In S. Koyejo,
 631 S. Mohamed, A. Agarwal, D. Belgrave, K. Cho, and A. Oh (eds.), *Advances in Neural Information
 632 Processing Systems*, volume 35, pp. 6219–6235. Curran Associates, Inc., 2022.

633

634 Yanghao Li, Naiyan Wang, Jianping Shi, Jiaying Liu, and Xiaodi Hou. Revisiting batch normalization
 635 for practical domain adaptation, 2016. URL <https://arxiv.org/abs/1603.04779>.

636

637 Carole L. Marcus, Reneé H. Moore, Carol L. Rosen, Bruno Giordani, Susan L. Garetz, H. Gerry
 638 Taylor, Ron B. Mitchell, Raouf Amin, Eliot S. Katz, Raanan Arens, Shalini Paruthi, Hiren
 639 Muzumdar, David Gozal, Nina Hattiangadi Thomas, Janice Ware, Dean Beebe, Karen Snyder, Lisa
 640 Elden, Robert C. Sprecher, Paul Willging, Dwight Jones, John P. Bent, Timothy Hoban, Ronald D.
 641 Chervin, Susan S. Ellenberg, Susan Redline, and Childhood Adenotonsillectomy Trial (CHAT). A
 642 randomized trial of adenotonsillectomy for childhood sleep apnea. *The New England Journal of
 643 Medicine*, 368(25):2366–2376, June 2013. ISSN 1533-4406. doi: 10.1056/NEJMoa1215881.

644

645 Jose G. Moreno-Torres, Troy Raeder, Rocío Alaiz-Rodríguez, Nitesh V. Chawla, and Francisco
 646 Herrera. A unifying view on dataset shift in classification. *Pattern Recognition*, 45(1):521–530,
 647 2012. ISSN 0031-3203. doi: <https://doi.org/10.1016/j.patcog.2011.06.019>.

648

649 Christian O'Reilly, Nadia Gosselin, and Julie Carrier. Montreal archive of sleep studies: an open-
 650 access resource for instrument benchmarking and exploratory research. *Journal of sleep research*,
 651 23, 06 2014. doi: 10.1111/jsr.12169.

648 A. Paszke, S. Gross, F. Massa, A. Lerer, J. Bradbury, G. Chanan, T. Killeen, Z. Lin, N. Gimelshein,
 649 L. Antiga, A. Desmaison, A. Kopf, E. Yang, Z. DeVito, M. Raison, A. Tejani, S. Chilamkurthy,
 650 B. Steiner, L. Fang, J. Bai, and S. Chintala. Pytorch: An imperative style, high-performance deep
 651 learning library. In *Advances in Neural Information Processing Systems (NeurIPS)*, pp. 8024–8035.
 652 Curran Associates, Inc., 2019.

653 Mathias Perslev, Michael Jensen, Sune Darkner, Poul Jørgen Jennum, and Christian Igel. U-time: A
 654 fully convolutional network for time series segmentation applied to sleep staging. *Advances in
 655 Neural Information Processing Systems*, 32, 2019.

656 Mathias Perslev, Sune Darkner, Lykke Kempfner, Miki Nikolic, Poul Jennum, and Christian Igel.
 657 U-Sleep: resilient high-frequency sleep staging. *npj Digital Medicine*, 4:72, 04 2021. doi:
 658 10.1038/s41746-021-00440-5.

659 Huy Phan, Fernando Andreotti, Navin Cooray, Oliver Y. Chén, and Maarten De Vos. SeqSleepNet:
 660 End-to-End Hierarchical Recurrent Neural Network for Sequence-to-Sequence Automatic Sleep
 661 Staging, February 2019. URL <http://arxiv.org/abs/1809.10932>. arXiv:1809.10932.

662 Huy Phan, Oliver Y. Chen, Minh C. Tran, Philipp Koch, Alfred Mertins, and Maarten De Vos.
 663 XSleepNet: Multi-view sequential model for automatic sleep staging. *IEEE Transactions on
 664 Pattern Analysis and Machine Intelligence*, 44(09):5903–5915, sep 2022a. ISSN 1939-3539. doi:
 665 10.1109/TPAMI.2021.3070057.

666 Huy Phan, Kaare Mikkelsen, Oliver Y. Chén, Philipp Koch, Alfred Mertins, and Maarten De Vos.
 667 Sleeptransformer: Automatic sleep staging with interpretability and uncertainty quantification.
 668 *IEEE Transactions on Biomedical Engineering*, 69(8):2456–2467, 2022b. doi: 10.1109/TBME.
 669 2022.3147187.

670 Huy Phan, Kristian P. Lorenzen, Elisabeth Heremans, Oliver Y. Chén, Minh C. Tran, Philipp
 671 Koch, Alfred Mertins, Mathias Baumert, Kaare B. Mikkelsen, and Maarten De Vos. L-
 672 SeqSleepNet: Whole-cycle Long Sequence Modeling for Automatic Sleep Staging. *IEEE Journal
 673 of Biomedical and Health Informatics*, 27(10):4748–4757, October 2023. ISSN 2168-2208.
 674 doi: 10.1109/JBHI.2023.3303197. URL <https://ieeexplore.ieee.org/document/10210638/?arnumber=10210638>. Conference Name: IEEE Journal of Biomedical and
 675 Health Informatics.

676 Stuart Quan, Barbara Howard, Conrad Iber, James Kiley, F. Nieto, George O’Connor, David Rapoport,
 677 Susan Redline, John Robbins, Jonathan Samet, and Patricia Wahl. The sleep heart health study:
 678 Design, rationale, and methods. *Sleep*, 20:1077–85, 01 1998. doi: 10.1093/sleep/20.12.1077.

679 S. Redline, P. V. Tishler, T. D. Tosteson, J. Williamson, K. Kump, I. Browner, V. Ferrette, and
 680 P. Krejci. The familial aggregation of obstructive sleep apnea. *American Journal of Respiratory
 681 and Critical Care Medicine*, 151(3 Pt 1):682–687, March 1995. ISSN 1073-449X. doi: 10.1164/
 682 ajrccm/151.3_Pt_1.682.

683 Olaf Ronneberger, Philipp Fischer, and Thomas Brox. U-net: Convolutional networks for biomedical
 684 image segmentation. In *Medical image computing and computer-assisted intervention—MICCAI
 685 2015: 18th international conference, Munich, Germany, October 5-9, 2015, proceedings, part III*
 686 18, pp. 234–241. Springer, 2015.

687 Carol L. Rosen, Emma K. Larkin, H. Lester Kirchner, Judith L. Emancipator, Sarah F. Bivins, Susan A.
 688 Surovec, Richard J. Martin, and Susan Redline. Prevalence and risk factors for sleep-disordered
 689 breathing in 8- to 11-year-old children: association with race and prematurity. *The Journal of
 690 Pediatrics*, 142(4):383–389, April 2003. ISSN 0022-3476. doi: 10.1067/mpd.2003.28.

691 Carol L. Rosen, Dennis Auckley, Ruth Benca, Nancy Foldvary-Schaefer, Conrad Iber, Vishesh Kapur,
 692 Michael Rueschman, Phyllis Zee, and Susan Redline. A multisite randomized trial of portable
 693 sleep studies and positive airway pressure autotitration versus laboratory-based polysomnography
 694 for the diagnosis and treatment of obstructive sleep apnea: the HomePAP study. *Sleep*, 35(6):
 695 757–767, June 2012. ISSN 1550-9109. doi: 10.5665/sleep.1870.

702 Robin Tibor Schirrmeister, Jost Tobias Springenberg, Lukas Dominique Josef Fiederer, Martin
 703 Glasstetter, Katharina Eggensperger, Michael Tangermann, Frank Hutter, Wolfram Burgard, and
 704 Tonio Ball. Deep learning with convolutional neural networks for EEG decoding and visualization.
 705 *Human Brain Mapping*, 38(11):5391–5420, November 2017. ISSN 1065-9471, 1097-0193. doi:
 706 10.1002/hbm.23730. URL <http://arxiv.org/abs/1703.05051>. arXiv:1703.05051 [cs].

707 Adam P. Spira, Terri Blackwell, Katie L. Stone, Susan Redline, Jane A. Cauley, Sonia Ancoli-Israel,
 708 and Kristine Yaffe. Sleep-disordered breathing and cognition in older women. *Journal of the*
 709 *American Geriatrics Society*, 56(1):45–50, January 2008. ISSN 1532-5415. doi: 10.1111/j.
 710 1532-5415.2007.01506.x.

711 Jens B. Stephansen, Alexander N. Olesen, Mads Olsen, Aditya Ambati, Eileen B. Leary, Hyatt E.
 712 Moore, Oscar Carrillo, Ling Lin, Fang Han, Han Yan, Yun L. Sun, Yves Dauvilliers, Sabine
 713 Scholz, Lucie Barateau, Birgit Hogl, Ambra Stefani, Seung Chul Hong, Tae Won Kim, Fabio
 714 Pizza, Giuseppe Plazzi, Stefano Vandi, Elena Antelmi, Dimitri Perrin, Samuel T. Kuna, Paula K.
 715 Schweitzer, Clete Kushida, Paul E. Peppard, Helge B. D. Sorensen, Poul Jenum, and Emmanuel
 716 Mignot. Neural network analysis of sleep stages enables efficient diagnosis of narcolepsy. *Nature*
 717 *Communications*, 9(1), dec 2018. doi: 10.1038/s41467-018-07229-3.

718 Suzanne Stevens and Glenn Clark. Chapter 6 - polysomnography. In DAMIEN STEVENS (ed.),
 719 *Sleep Medicine Secrets*, pp. 45–63. Hanley & Belfus, 2004. ISBN 978-1-56053-592-8. doi:
 720 <https://doi.org/10.1016/B978-1-56053-592-8.50010-5>.

721 Baochen Sun and Kate Saenko. Deep CORAL: Correlation Alignment for Deep Domain Adaptation,
 722 July 2016. URL <http://arxiv.org/abs/1607.01719>. arXiv:1607.01719 [cs].

723 Akara Supratak, Hao Dong, Chao Wu, and Yike Guo. DeepSleepNet: A model for automatic sleep
 724 stage scoring based on raw single-channel EEG. *IEEE Transactions on Neural Systems and*
 725 *Rehabilitation Engineering*, 25(11):1998–2008, 2017.

726 Rahul Thapa, Magnus Ruud Kjær, Bryan He, Ian Covert, Hyatt Moore, Umaer Hanif, Gauri Ganjoo,
 727 M. Brandon Westover, Poul Jenum, Andreas Brink-Kjær, Emmanuel Mignot, and James Zou. A
 728 multimodal sleep foundation model developed with 500k hours of sleep recordings for disease
 729 predictions. pp. 2025.02.04.25321675. doi: 10.1101/2025.02.04.25321675. URL <https://www.ncbi.nlm.nih.gov/pmc/articles/PMC11838666/>.

730 D Ulyanov. Instance normalization: The missing ingredient for fast stylization. *arXiv preprint*
 731 *arXiv:1607.08022*, 2016.

732 Dequan Wang, Evan Shelhamer, Shaoteng Liu, Bruno Olshausen, and Trevor Darrell. Tent: Fully
 733 Test-time Adaptation by Entropy Minimization, March 2021. URL <http://arxiv.org/abs/2006.10726>. arXiv:2006.10726 [cs, stat].

734 Jiquan Wang, Sha Zhao, Haiteng Jiang, Yangxuan Zhou, Zhenghe Yu, Tao Li, Shijian Li, and Gang
 735 Pan. CareSleepNet: A hybrid deep learning network for automatic sleep staging. 28(12):7392–
 736 7405. ISSN 2168-2208. doi: 10.1109/JBHI.2024.3426939. URL <https://ieeexplore.ieee.org/document/10595067/>.

737 Peter Welch. The use of fast fourier transform for the estimation of power spectra: a method
 738 based on time averaging over short, modified periodograms. *IEEE Transactions on audio and*
 739 *electroacoustics*, 15(2):70–73, 1967.

740 Chaoqi Yang, M Westover, and Jimeng Sun. Biot: Biosignal transformer for cross-data learning
 741 in the wild. In A. Oh, T. Naumann, A. Globerson, K. Saenko, M. Hardt, and S. Levine (eds.),
 742 *Advances in Neural Information Processing Systems*, volume 36, pp. 78240–78260. Curran Asso-
 743 ciates, Inc., 2023. URL https://proceedings.neurips.cc/paper_files/paper/2023/file/f6b30f3e2dd9cb53bbf2024402d02295-Paper-Conference.pdf.

744 Shiqi Yang, Yaxing Wang, Joost Van De Weijer, Luis Herranz, and Shangling Jui. Generalized Source-
 745 free Domain Adaptation. In *2021 IEEE/CVF International Conference on Computer Vision (ICCV)*,
 746 pp. 8958–8967, Montreal, QC, Canada, October 2021. IEEE. ISBN 978-1-66542-812-5. doi:
 747 10.1109/ICCV48922.2021.00885. URL <https://ieeexplore.ieee.org/document/9710764/>.

756 Guo-Qiang Zhang, Licong Cui, Remo Mueller, Shiqiang Tao, Matthew Kim, Michael Rueschman,
757 Sara Mariani, Daniel Mobley, and Susan Redline. The National Sleep Research Resource: towards
758 a sleep data commons. *Journal of the American Medical Informatics Association: JAMIA*, 25(10):
759 1351–1358, October 2018. ISSN 1527-974X. doi: 10.1093/jamia/ocy064.
760
761
762
763
764
765
766
767
768
769
770
771
772
773
774
775
776
777
778
779
780
781
782
783
784
785
786
787
788
789
790
791
792
793
794
795
796
797
798
799
800
801
802
803
804
805
806
807
808
809

810
811
A APPENDIX812
813
**A.1 PROOF OF THE BURES-WASSERSTEIN GEODESIC (6) BETWEEN COVARIANCE MATRICES
814 OF STRUCTURE (2)**815
816 **Proposition A.1.** Let $\Sigma^{(s)}$ and $\Sigma^{(t)}$ be two covariance matrices in $\mathbb{R}^{cf \times cf}$ following (2). Let us
817 denote $\mathbf{P}^{(s)}$ and $\mathbf{P}^{(t)}$ the corresponding PSD matrices. The geodesic associated with the Bures-
818 Wasserstein metric between $\Sigma^{(s)}$ and $\Sigma^{(t)}$ and parameterized by $\alpha \in [0, 1]$ is $\Sigma(\alpha)$ following (2) of
819 PSD

820
821
822
$$\mathbf{P}(\alpha) = \left((1 - \alpha) \mathbf{P}^{(s)} \odot \frac{1}{2} + \alpha \mathbf{P}^{(t)} \odot \frac{1}{2} \right)^{\odot 2}.$$

823
824 *Proof.* From Bhatia et al. (2019), the geodesic associated with the Bures-Wasserstein metric between
825 two covariance matrices $\Sigma^{(s)}$ and $\Sigma^{(t)}$ is given by

826
827
828
$$\gamma(\alpha) = (1 - \alpha)^2 \Sigma^{(s)} + \alpha^2 \Sigma^{(t)} + \alpha(1 - \alpha) \left[(\Sigma^{(s)} \Sigma^{(t)})^{\frac{1}{2}} + (\Sigma^{(t)} \Sigma^{(s)})^{\frac{1}{2}} \right]. \quad (9)$$

829
830 where

831
832
833
$$(\Sigma^{(s)} \Sigma^{(t)})^{\frac{1}{2}} = \Sigma^{(s) \frac{1}{2}} \left(\Sigma^{(s) \frac{1}{2}} \Sigma^{(t)} \Sigma^{(s) \frac{1}{2}} \right)^{\frac{1}{2}} \Sigma^{(s) - \frac{1}{2}}. \quad (10)$$

834
835 Since $\Sigma^{(s)}$ and $\Sigma^{(t)}$ diagonalize in the unitary basis $\mathbf{I}_c \otimes \mathbf{F}_f$, $\gamma(\alpha)$ also diagonalizes in this basis.
836 Thus, we only have to compute the geodesic between the PSD matrices $\mathbf{P}^{(s)}$ and $\mathbf{P}^{(t)}$ and from now
837 on, all operations are element-wise. Let $\mathbf{P}(\alpha)$ be the PSD of $\gamma(\alpha)$, we have

838
839
840
$$\mathbf{P}(\alpha) = (1 - \alpha)^2 \mathbf{P}^{(s)} + \alpha^2 \mathbf{P}^{(t)} + \alpha(1 - \alpha) \left[(\mathbf{P}^{(s)} \odot \mathbf{P}^{(t)})^{\odot \frac{1}{2}} + (\mathbf{P}^{(t)} \odot \mathbf{P}^{(s)})^{\odot \frac{1}{2}} \right] \quad (11)$$

841
842
843
$$= (1 - \alpha)^2 \mathbf{P}^{(s)} + \alpha^2 \mathbf{P}^{(t)} + 2\alpha(1 - \alpha) (\mathbf{P}^{(s)} \odot \mathbf{P}^{(t)})^{\odot \frac{1}{2}} \quad (12)$$

844
845
846
$$= \left((1 - \alpha) \mathbf{P}^{(s) \odot \frac{1}{2}} + \alpha \mathbf{P}^{(t) \odot \frac{1}{2}} \right)^{\odot 2}. \quad (13)$$

847
848 This concludes the proof. ■849
850
A.2 BALANCED DATASETS851
852
Table 3: Number of samples in the balanced datasets. Average and standard deviation (across LODO)
853 are computed over 10 datasets left-out from the training set.854
855
856
857
858
859
860
861
862
863

Balanced datasets	Number of subjects
Balanced@40	360 ± 0
Balanced@100	787 ± 19
Balanced@200	1387 ± 63
Balanced@400	2466 ± 157
All subjects	9929 ± 1659

864
865 In the main paper, we report results across different training set sizes. Since the datasets are highly
866 imbalanced (e.g., ABC has 44 subjects, SHHS has 5,730), we create balanced subsets by randomly
867 selecting up to N subjects per dataset. This avoids over-representing the largest dataset and ensures
868 greater diversity in the training data. We consider four values of N : 40, 100, 200, and 400. The
869 average number of subjects in each balanced set is shown in Table 3. Notably, the balanced set with
870 400 subjects contains roughly four times less data than the full dataset.871
872
A.3 U-TIME: CNN FOR TIME SERIES SEGMENTATION873
874 U-Time Perslev et al. (2019; 2021) is a convolutional neural network (CNN) inspired by the U-Net
875 architecture Ronneberger et al. (2015), designed for segmenting temporal sequences. U-Time maps

864 sequential inputs of arbitrary length to sequences of class labels on a freely chosen temporal scale.
 865 The architecture is composed of several encoder and decoder blocks, with skip connections between
 866 them.
 867

868 **Encoder blocks** A single encoder block is composed of a convolutional layer, an activation
 869 function, a BatchNorm layer, and a max pooling layer. First, the convolution is applied to the input
 870 signal, followed by the activation function and the BatchNorm layer. Finally, the max pooling
 871 layer downsamples the temporal dimension. In the following, the pre-BatchNorm feature map is
 872 denoted \mathbf{G} and the post-BatchNorm feature map $\tilde{\mathbf{G}}$, *i.e.*, $\tilde{\mathbf{G}} \triangleq \text{BatchNorm}(\mathbf{G})$. Each encoder block
 873 downsamples by 2 the signal length but increases the number of channels.
 874

875 **Decoder blocks and Segmentation Head** The decoding part of U-Time is symmetrical to the
 876 encoding part. Each decoder block doubles the signal length and decreases the number of channels.
 877 It is composed of a convolutional layer, an activation function, a BatchNorm layer, an upsampling
 878 layer and a concatenation layer of the skip connection of the corresponding encoding block. Finally,
 879 the segmentation head applies two convolutional layers with an activation function in between to
 880 output the final segmentation. It should be noted that U-Time employs BatchNorm layers but other
 881 normalization layers, such as LayerNorm Ba et al. (2016) or InstanceNorm Ulyanov (2016) are
 882 possible.
 883

884 **Implementation** The architecture is inspired from Braindecode Schirrmeister et al. (2017). The
 885 implementation is improved to make it more efficient and faster. One epoch of training takes about
 886 30 min on a single H100 GPU.
 887

A.4 ARCHITECTURE: CNNTRANSFORMER

888 The CNNTransformer is a hybrid architecture designed for multichannel time series classification
 889 inspired by transformers for EEG-Data Wang et al.; Phan et al. (2022b); Yang et al. (2023); Thapa et al..
 890 It combines convolutional feature extraction with long-range temporal modeling via a Transformer
 891 encoder at epoch-level. The model processes an input tensor of shape (B, S, C, T) , where B is the
 892 batch size, S is the number of temporal segments, C is the number of input channels, and T is the
 893 number of time samples per segment. It outputs a tensor of shape $(B, n_{\text{classes}}, S)$, where n_{classes} is the
 894 number of classes and S is the number of epochs.
 895

896 The architecture consists of the following components:
 897

- 898 • **Reshaping:** The input is first permuted and reshaped to a 3D tensor of shape $(B, C, S \cdot T)$
 899 to be compatible with 1D convolutional layers applied along the temporal dimension.
 900
- 901 • **CNN-based Feature Extractor:** A stack of 10 Conv1D layers, each followed by ELU
 902 activation and Batch Normalization. Some layers use a stride greater than 1 to progressively
 903 reduce the temporal resolution. This block extracts local temporal patterns and increases the
 904 representational capacity up to a dimensionality of d_{model} .
 905
- 906 • **Adaptive Pooling:** An AdaptiveAvgPool1D layer reduces the temporal length to a fixed
 907 number of steps (S), independent of the input sequence length. This step ensures a consistent
 908 temporal resolution before the Transformer.
 909
- 910 • **Positional Encoding:** Learnable positional embeddings of shape $(1, S, d_{\text{model}})$ are added
 911 to the feature representations to preserve temporal ordering before passing through the
 912 Transformer encoder.
 913
- 914 • **Transformer Encoder:** A standard Transformer encoder composed of L layers, each
 915 consisting of multi-head self-attention and a feedforward sublayer. This module models
 916 global temporal dependencies across the S steps.
 917
- 918 • **Classification Head:** After transposing the data to shape (B, d_{model}, S) , a final 1D convolution
 919 with a kernel size of 1 projects the output to n_{classes} , yielding predictions for each epoch
 920 segment.
 921

922 The model is trained end-to-end using standard optimization techniques. The use of adaptive pooling
 923 and self-attention enables it to generalize across variable-length inputs while maintaining temporal
 924 resolution. A full summary of the architecture is provided in Table 4.
 925

918
919
920
Table 4: Architecture overview of the CNNTransformer model. In practice, d_{model} is set to 768, n_{head}
to 8, and S is 35.

921 Stage	922 Operation	923 Details	924 Output Shape
922 Input	923 Raw signal	924 Multichannel EEG signal with S segments and T time samples per segment	925 (B, S, C, T)
924 Reshape	925 Permute & flatten	926 Rearranged as $(B, C, S \cdot T)$ to process with 1D convolutions	927 $(B, C, S \cdot T)$
926 Feature Extractor	927 1D CNN stack	928 10-layer sequence of Conv1D \rightarrow ELU \rightarrow Batch-Norm; includes temporal downsampling via stride	929 $(B, d_{\text{model}}, T')$
928 Temporal Pooling	929 AdaptiveAvgPool1D	930 Downsamples to fixed temporal resolution defined by S	931 (B, d_{model}, S)
930 Positional Encoding	931 Learnable embeddings	932 Added to temporal dimension to encode temporal order before transformer layers	933 (B, d_{model}, S)
931 Transformer Encoder	932 Multi-head attention	933 2 Transformer layers with d_{model} embedding dimension, n_{head} heads, and feedforward sublayers	934 (B, d_{model}, S)
932 Classifier	933 Linear projection	934 Projects feature vectors to class logits at each epoch time step	935 $(B, n_{\text{classes}}, S)$

936
937
A.5 EQUATION FOR BATCHNORM AND INSTANCENORM938
939
940
941
BatchNorm The BatchNorm layer Ioffe & Szegedy (2015) normalizes features maps in a neural network to have zero mean and unit variance. At train time, given a batch $\mathcal{B} = \{\mathbf{G}^{(1)}, \dots, \mathbf{G}^{(N)}\} \subset \mathbb{R}^{c \times \ell}$ of N pre-BatchNorm feature maps and for all $j, m, l \in \llbracket 1, N \rrbracket \times \llbracket 1, c \rrbracket \times \llbracket 1, \ell \rrbracket$, the BatchNorm layer is computed as

938
939
940
941
942
943
944
$$\tilde{G}_{m,l}^{(j)} = \gamma_m \frac{G_{m,l}^{(j)} - \hat{\mu}_m}{\sqrt{\hat{\sigma}_m^2 + \varepsilon}} + \beta_m, \quad (14)$$

945
946
where $\gamma, \beta \in \mathbb{R}^c$ are learnable parameters. The mean and standard deviation $\hat{\mu} \in \mathbb{R}^c$ and $\hat{\sigma} \in \mathbb{R}^c$ are computed across the time and the batch,

947
948
949
950
951
952
$$\begin{aligned} \hat{\mu}_m &\triangleq \frac{1}{N\ell} \sum_{j=1}^N \sum_{l=1}^{\ell} G_{m,l}^{(j)}, \\ \hat{\sigma}_m^2 &\triangleq \frac{1}{N\ell} \sum_{j=1}^N \sum_{l=1}^{\ell} (G_{m,l}^{(j)} - \hat{\mu}_m)^2. \end{aligned} \quad (15)$$

953
954
At test time, the mean and variance $\hat{\mu}$ and $\hat{\sigma}$ are replaced by their running mean and variance, also called exponential moving average, estimated during training.955
956
957
InstanceNorm Another popular normalization is the InstanceNorm layer Ulyanov (2016). During training, InstanceNorm operates similarly to (14), but the mean and variance are computed per sample instead of across the batch dimension, *i.e.*, $\hat{\mu}_m^{(j)}$ and $\hat{\sigma}_m^{(j)}$ are computed for each sample j ,

958
959
960
961
962
963
964
$$\begin{aligned} \hat{\mu}_m^{(j)} &\triangleq \frac{1}{\ell} \sum_{l=1}^{\ell} G_{m,l}^{(j)}, \\ (\hat{\sigma}_m^{(j)})^2 &\triangleq \frac{1}{\ell} \sum_{l=1}^{\ell} (G_{m,l}^{(j)} - \hat{\mu}_m^{(j)})^2. \end{aligned} \quad (16)$$

965
966
Hence, each sensor of each sample is normalized independently of the others. At test time, InstanceNorm behaves identically to its training phase and therefore does not rely on running statistics contrary to the BatchNorm.968
969
A.6 SENSITIVITY TO FILTER SIZE970
971
The filter size f in PSDNorm controls the temporal context used for normalization, influencing the strength of adaptation to temporal variations. Figure 6 shows the impact of different f values on the

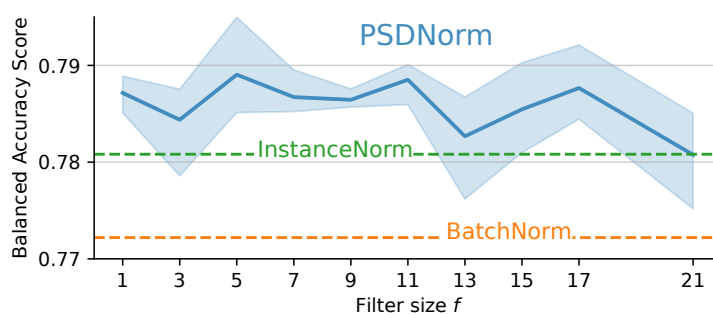


Figure 6: **Performance of PSDNorm with varying filter sizes.** The BACC score is plotted against the filter size used with U-Sleep.

BACC score across datasets using U-Sleep trained on balanced@400. This experiments shows that for any f , PSDNorm consistently improves performance compared to other normalization techniques. Taking a f between 5 and 11 yields the best results, with a peak at $f = 5$. Smaller values (e.g., $f = 1$, equivalent to InstanceNorm) provide less adaptation, while larger values (e.g., $f = 21$) may over-smooth temporal variations, leading to diminished performance. Overall, the results shows that f is not so sensitive yielding good performance for a wide range of values.

A.7 F1 SCORE VS. BALANCED ACCURACY

In the main paper, we report Balanced Accuracy scores, which account for class imbalance in sleep stage classification. Prior work, such as the U-Time paper Perslev et al. (2019), uses the F1 score to evaluate performance. In Table 5, we report F1 scores on the left-out datasets. These scores are slightly higher than the Balanced Accuracy scores and are comparable to those reported in the U-Time paper.

Our main findings remain consistent: BatchNorm and InstanceNorm are the strongest baselines and achieve the best performance on 3 out of 10 datasets. PSDNorm outperforms all other methods on 7 out of 10 datasets. The same trend holds for the balanced@400 setup, where PSDNorm again outperforms all baselines on 7 datasets, while InstanceNorm is never the top performer.

These results confirm that our implementation achieves state-of-the-art performance in sleep stage classification. Moreover, PSDNorm maintains its advantage even in data-limited settings

A.8 IMPACT OF WHITENING AND TARGET COVARIANCE

As explained in the main paper, InstanceNorm is a special case of PSDNorm with $F = 1$ and an identity target covariance matrix (i.e., whitening). PSDNorm extends this by (i) using temporal context with $F > 1$, and (ii) mapping the PSD to a target covariance matrix, such as a barycenter (i.e., colorization).

In this section, we evaluate the impact of whitening on the performance of PSDNorm, to assess the benefit of using a barycenter as the target covariance matrix. Table 6 reports results on 10 datasets (balanced@400), with and without whitening.

Whitening improves performance on only one dataset (CCSHS), while projecting to the barycenter yields the best results on 6 datasets.

This suggests that, while whitening may help when $F = 1$, it is less effective when $F > 1$. Using a barycenter leads to a more robust and stable target covariance matrix.

A.9 GENERALIZATION OF PSDNORM IN CNNTRANSFORMER

The CNNTransformer architecture is a hybrid model that combines convolutional and transformer layers for time series classification.

Table 5: **F1 scores of different methods on the left-out datasets.** The lower section displays results for training over datasets balanced @400 *i.e.*, **small-scale dataset**, while the upper section presents results for training over all subjects *i.e.*, **large-scale dataset**. The best scores are highlighted in **bold**. The reported standard deviations indicate performance variability across 3 seeds.

	Dataset	BatchNorm	LayerNorm	InstanceNorm	TMA	PSDNorm(F=5)
All subjects	ABC	81.00 \pm 0.11	79.50 \pm 0.49	80.56 \pm 0.39	80.89 \pm 0.06	81.12\pm0.37
	CCSHS	89.83\pm0.19	89.01 \pm 0.43	89.39 \pm 0.16	89.37 \pm 0.11	89.13 \pm 0.17
	CFS	88.30 \pm 0.52	87.39 \pm 0.06	88.45 \pm 0.17	88.28 \pm 0.37	88.52\pm0.15
	CHAT	65.77 \pm 4.06	65.25 \pm 3.96	71.35 \pm 2.75	71.80 \pm 2.66	72.16\pm2.21
	HOMEPA	77.06 \pm 0.14	76.62 \pm 1.06	77.50 \pm 0.46	77.82\pm0.64	77.30 \pm 0.24
	MASS	77.27 \pm 1.42	74.21 \pm 2.05	75.12 \pm 2.08	77.74\pm1.05	76.00 \pm 3.00
	MROS	85.53\pm0.48	84.02 \pm 0.95	85.22 \pm 0.19	85.13 \pm 0.98	85.02 \pm 0.42
	PhysioNet	74.98 \pm 1.84	74.29 \pm 1.50	75.07 \pm 1.05	76.01\pm0.73	75.29 \pm 1.21
	SHHS	78.95 \pm 0.92	78.04 \pm 1.21	80.30 \pm 1.29	78.84 \pm 0.43	80.32\pm0.91
	SOF	86.30 \pm 0.40	85.82 \pm 0.22	86.57 \pm 0.60	86.31 \pm 0.27	86.99\pm0.33
Balanced@400	Mean(Dataset)	80.50 \pm 0.51	79.41 \pm 0.73	80.95 \pm 0.36	81.22\pm0.20	81.19 \pm 0.11
	Mean(Subject)	80.05 \pm 0.78	79.09 \pm 0.90	81.31 \pm 0.83	80.59 \pm 0.19	81.39\pm0.69
	ABC	79.80\pm0.34	77.86 \pm 0.80	78.36 \pm 1.20	79.49 \pm 0.68	78.08 \pm 0.78
	CCSHS	88.32 \pm 0.49	87.22 \pm 0.51	88.73 \pm 0.52	88.47 \pm 0.62	88.79\pm0.99
	CFS	87.01 \pm 0.18	85.61 \pm 0.16	87.62\pm0.27	87.37 \pm 0.44	87.06 \pm 0.77
	CHAT	66.56 \pm 1.42	61.32 \pm 2.25	64.19 \pm 4.63	69.90 \pm 2.74	71.86\pm0.95
	HOMEPA	76.20 \pm 1.25	76.15 \pm 1.13	77.66 \pm 0.58	76.83 \pm 0.97	77.85\pm1.29
	MASS	76.06 \pm 1.69	73.95 \pm 5.80	76.94 \pm 1.12	76.32 \pm 0.36	77.16\pm1.73
	MROS	83.69 \pm 0.39	82.22 \pm 1.27	83.95 \pm 0.53	84.15\pm0.46	83.51 \pm 0.84
	PhysioNet	76.26\pm1.27	70.40 \pm 0.14	73.84 \pm 0.93	75.24 \pm 2.72	73.51 \pm 3.05
Mean(Dataset)	SHHS	76.98 \pm 0.70	75.98 \pm 0.22	79.12 \pm 0.96	78.19 \pm 0.90	79.26\pm1.35
	SOF	85.49 \pm 0.58	84.23 \pm 1.30	85.50 \pm 0.86	85.56\pm0.90	84.14 \pm 1.05
Mean(Subject)	Mean(Dataset)	79.64 \pm 0.41	77.57 \pm 0.73	79.59 \pm 0.25	80.15\pm0.26	80.12 \pm 0.57
	Mean(Subject)	78.57 \pm 0.55	76.86 \pm 0.22	79.53 \pm 0.30	79.70 \pm 0.66	80.29\pm0.68

Table 6: Impact of the whitening on the performance of PSDNorm on the 10 datasets balanced @ 400.

Dataset	BatchNorm	InstanceNorm	PSDNorm	
			Barycenter	Whitening
ABC	78.26 \pm 1.33	78.73\pm0.42	78.18 \pm 0.68	77.86 \pm 1.33
CCSHS	87.42 \pm 0.16	87.62 \pm 0.42	87.58 \pm 0.30	87.80\pm0.23
CFS	84.32 \pm 0.57	84.72\pm0.33	84.29 \pm 0.36	84.01 \pm 0.60
CHAT	66.55 \pm 0.88	64.43 \pm 4.41	70.28\pm1.70	69.07 \pm 3.73
HOMEPA	75.25 \pm 0.50	76.47 \pm 0.63	76.83\pm0.61	76.13 \pm 0.93
MASS	70.00 \pm 1.91	71.52 \pm 1.13	72.77\pm1.09	69.11 \pm 1.51
MROS	80.37 \pm 0.20	80.28 \pm 0.21	80.26 \pm 0.11	80.50\pm0.75
PhysioNet	75.81\pm0.13	74.68 \pm 0.55	74.82 \pm 2.11	74.58 \pm 1.57
SHHS	76.44 \pm 0.92	78.68 \pm 0.37	78.88\pm0.68	78.77 \pm 0.67
SOF	81.08 \pm 1.14	80.68 \pm 1.38	79.49 \pm 0.41	80.10 \pm 0.62
Mean	77.55 \pm 0.34	77.78 \pm 0.46	78.34\pm0.42	77.79 \pm 0.30

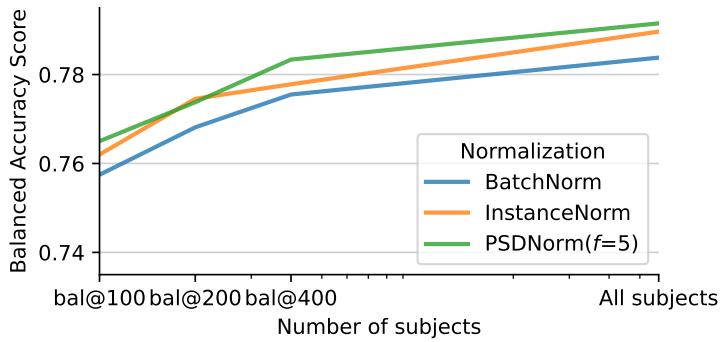
The main paper presents a critical difference diagram for the CNNTransformer evaluated on datasets balanced@400. It shows that PSDNorm with $F = 5$ is the best-performing normalization layer.

In Table 7, we report the results of different normalization layers used in the CNNTransformer architecture on datasets balanced@400.

1080 Table 7: Different normalization layers used in the CNNTransformer architecture for datasets
 1081 balanced@400.

1082

1083 Dataset	1084 BatchNorm	1085 InstanceNorm	1086 TMA	1087 PSDNorm
1088 ABC	1089 76.99 ± 0.53	1090 75.40 ± 0.36	1091 77.50 ± 0.54	1092 76.31 ± 0.46
1093 CCSHS	1094 86.75 ± 0.48	1095 87.00 ± 0.34	1096 86.73 ± 0.25	1097 86.92 ± 0.32
1098 CFS	1099 83.32 ± 0.35	1100 83.77 ± 0.34	1101 83.16 ± 0.38	1102 83.71 ± 0.29
1103 CHAT	1104 66.44 ± 0.49	1105 66.40 ± 2.55	1106 66.47 ± 1.37	1107 70.04 ± 0.37
1108 HOMEPA	1109 74.81 ± 1.36	1110 75.92 ± 0.44	1111 74.76 ± 0.83	1112 75.26 ± 0.55
1113 MASS	1114 71.51 ± 0.47	1115 71.70 ± 1.17	1116 70.57 ± 0.80	1117 72.55 ± 0.81
1118 MROS	1119 79.77 ± 0.31	1120 79.74 ± 0.55	1121 79.85 ± 0.08	1122 79.77 ± 0.30
1123 PhysioNet	1124 72.54 ± 0.34	1125 74.36 ± 0.84	1126 71.39 ± 1.38	1127 74.95 ± 0.41
1128 SHHS	1129 75.34 ± 0.34	1130 76.55 ± 0.92	1131 75.15 ± 0.98	1132 77.26 ± 0.57
1133 SOF	1134 80.63 ± 0.60	1135 80.78 ± 0.54	1136 81.03 ± 0.48	1137 80.31 ± 0.90
1138				
1139 Mean		1140 76.38 ± 0.17	1141 77.07 ± 0.28	1142 76.30 ± 0.57
1143				
1144				



1108 Figure 7: **Performance of PSDNorm and BatchNorm with varying training set sizes.** The BACC
 1109 score is plotted against the number of training subjects used with U-Sleep.

1110

1111 First, we observe that CNNTransformer performs slightly below U-Sleep. Second, BatchNorm and
 1112 InstanceNorm are the best performers on one and two datasets respectively, while PSDNorm achieves
 1113 the best performance on 7 out of 10 datasets.

1114

1115 PSDNorm with $F = 5$ outperforms BatchNorm by a margin of 0.9 and InstanceNorm by 0.54 in
 1116 average score.

1117

1118 These results highlight that PSDNorm is a plug-and-play normalization layer that can be seamlessly
 1119 integrated into various architectures to reduce feature space variability.

1120

A.10 EVOLUTION OF PERFORMANCE WITH TRAINING SET SIZE

1121

1122 The choice of f in PSDNorm controls the intensity of the normalization: larger f provide stronger
 1123 normalization, while smaller f allow more flexibility in the model. In Figure 7, we evaluate its impact
 1124 across different training set sizes and observe a clear trend: when trained on fewer subjects, larger
 1125 filter sizes yield better performance (*i.e.*, $f = 17$), whereas smaller filter sizes are more effective with
 1126 larger datasets (*i.e.*, $f = 5$). This suggests that with limited data, stronger normalization helps prevent
 1127 overfitting, while with more data, a more flexible model is preferred. On average, PSDNorm with
 1128 $f = 5$ offers a good compromise, achieving one of the best performances across all training set sizes.

1129

A.11 CRITICAL DIFFERENCE DIAGRAM FOR U-SLEEP ON ALL SUBJECTS

1130

1131 The main paper presents the critical difference diagram for U-Sleep on the dataset balanced@400.
 1132 Figure 8 extends this analysis to all subjects across datasets. The conclusion remains consistent:
 1133 PSDNorm with $F = 5$ is the best-performing normalization layer, while BatchNorm performs the

worst. Interestingly, PSDNorm with $F = 17$ ranks second to last, suggesting that overly strong adaptation can hurt performance when the dataset is large.

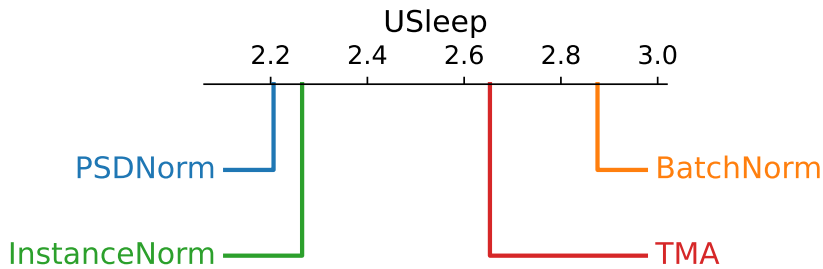


Figure 8: Critical difference diagram for U-Sleep on all subjects.

A.12 COMPUTATIONAL TIME OF PSDNORM

Table 8: **Computational time of PSDNorm compared to BatchNorm and InstanceNorm for USleep and CNNTransformer.** The time is done for leave out the dataset CHAT and with the dataset balanced @400. The time is averaged over 3 runs and reported in seconds.

Model	Normalization	Time per epoch (sec)	Time of inference (sec)
USleep	BatchNorm	161.94 ± 10.18	95.63 ± 4.85
USleep	InstanceNorm	$258.71 \pm 2.15(*)$	93.40 ± 8.18
USleep	PSDNorm($f = 5$)	172.85 ± 4.05	98.72 ± 12.09
CNNTransformer	BatchNorm	130.88 ± 2.67	93.03 ± 5.25
CNNTransformer	InstanceNorm	127.47 ± 5.14	92.70 ± 4.11
CNNTransformer	PSDNorm($f = 5$)	152.83 ± 2.29	92.57 ± 2.64

One important aspect of normalization layers is their computational cost, which can impact training and inference times. Table 8 compares the computational time of PSDNorm with BatchNorm and InstanceNorm in both U-Sleep and CNNTransformer architectures. In U-Sleep, PSDNorm takes 172.85 seconds per epoch, which is slightly higher than BatchNorm (161.94 seconds) but significantly lower than InstanceNorm (258.71 seconds). The high cost of InstanceNorm is due to the fact that the `torch.compile` was not working for Usleep and InstanceNorm. For inference, PSDNorm takes 98.72 seconds, which is comparable to BatchNorm (95.63 seconds) but slightly higher than InstanceNorm (93.40 seconds).

In CNNTransformer, PSDNorm takes 152.83 seconds per epoch, which is higher than BatchNorm (130.88 seconds) and InstanceNorm (127.47 seconds). However, for inference, PSDNorm is equivalent to both BatchNorm and InstanceNorm. The modest computational overhead introduced by PSDNorm is a worthwhile trade-off for its superior performance. This efficiency is enabled by the highly optimized implementation of the Fast Fourier Transform (FFT) on GPUs.

A.13 CLASS-WISE PERFORMANCE

The Tables show that the most complicated sleep stage to classify is N1, with F1 scores consistently lower than other stages across all normalization methods. This is likely due to the inherent difficulty of distinguishing N1 from other stages, as it shares characteristics with both wakefulness and deeper sleep stages. In contrast, stages like Wake and REM tend to have higher F1 scores, indicating that they are easier to classify accurately.

Figure 9 illustrates the class-wise F1 score differences between normalization layers score against BatchNorm score. For almost all the classes, other normalization increase the performance compared to BatchNorm except for N1 where InstanceNorm shows a decrease in performance. PSDNorm is consistently the best performing normalization across all classes, highlighting its effectiveness in

1188

1189

1190 Table 9: Class-wise F1 scores for BatchNorm layer on datasets balanced @ 400.

1191

Dataset	Wake	N1	N2	N3	REM	F1
ABC	86.07 \pm 0.68	53.97 \pm 0.36	80.05 \pm 0.52	71.35 \pm 1.45	88.43 \pm 0.13	79.80 \pm 0.34
CCSHS	95.22 \pm 0.46	48.08 \pm 2.87	84.88 \pm 0.81	86.13 \pm 1.01	88.54 \pm 0.93	88.32 \pm 0.49
CFS	94.64 \pm 0.10	42.69 \pm 0.39	82.27 \pm 0.75	77.20 \pm 0.30	86.94 \pm 0.34	87.01 \pm 0.18
CHAT	78.35 \pm 1.31	35.57 \pm 2.64	52.63 \pm 2.77	72.67 \pm 1.25	76.12 \pm 1.50	66.56 \pm 1.42
HOMEPA	84.51 \pm 1.01	41.45 \pm 0.71	73.88 \pm 2.00	57.41 \pm 1.72	82.52 \pm 1.33	76.20 \pm 1.25
MASS	66.93 \pm 4.65	40.02 \pm 2.00	78.73 \pm 0.67	67.01 \pm 0.39	75.80 \pm 5.65	76.06 \pm 1.69
MROS	94.63 \pm 0.25	41.73 \pm 1.11	73.74 \pm 0.72	47.86 \pm 0.33	82.70 \pm 0.46	83.69 \pm 0.39
PhysioNet	89.22 \pm 0.49	46.01 \pm 0.90	73.93 \pm 3.04	55.04 \pm 1.56	77.30 \pm 0.61	76.26 \pm 1.27
SHHS	85.68 \pm 1.57	32.56 \pm 1.34	72.48 \pm 2.00	61.91 \pm 1.31	79.09 \pm 1.07	76.98 \pm 0.70
SOF	93.91 \pm 0.15	38.29 \pm 1.09	79.15 \pm 0.57	71.86 \pm 3.17	86.49 \pm 0.18	85.49 \pm 0.58
Mean	86.91 \pm 1.07	42.04 \pm 1.34	75.17 \pm 1.39	66.84 \pm 1.25	82.39 \pm 1.22	79.64 \pm 0.83

1204

1205

1206

1207

1208

1209

Table 10: Class-wise F1 scores for LayerNorm layer with $f = 5$ on datasets balanced @ 400.

Dataset	Wake	N1	N2	N3	REM	F1
ABC	83.29 \pm 2.94	52.93 \pm 0.96	78.07 \pm 1.04	68.91 \pm 2.93	85.05 \pm 0.81	77.86 \pm 0.80
CCSHS	93.66 \pm 0.40	40.68 \pm 1.11	84.80 \pm 1.28	86.46 \pm 0.82	85.39 \pm 0.62	87.22 \pm 0.51
CFS	93.78 \pm 0.50	38.56 \pm 2.07	81.15 \pm 0.11	75.39 \pm 1.77	83.68 \pm 0.90	85.61 \pm 0.16
CHAT	72.07 \pm 2.84	30.11 \pm 0.63	46.82 \pm 6.98	70.45 \pm 2.92	68.11 \pm 4.07	61.32 \pm 2.25
HOMEPA	83.58 \pm 1.72	43.85 \pm 1.55	73.97 \pm 1.76	57.54 \pm 1.92	79.16 \pm 1.19	76.15 \pm 1.13
MASS	60.73 \pm 4.02	40.56 \pm 0.87	77.39 \pm 6.28	65.91 \pm 4.01	69.92 \pm 10.53	73.95 \pm 5.80
MROS	94.12 \pm 0.10	38.41 \pm 2.21	71.48 \pm 3.66	47.85 \pm 0.37	79.05 \pm 0.66	82.22 \pm 1.27
PhysioNet	88.04 \pm 0.37	44.72 \pm 2.03	64.53 \pm 1.93	48.49 \pm 0.54	68.17 \pm 7.15	70.40 \pm 0.14
SHHS	84.61 \pm 2.49	32.89 \pm 1.92	72.02 \pm 2.48	61.13 \pm 1.59	75.63 \pm 0.63	75.98 \pm 0.22
SOF	93.24 \pm 0.27	35.61 \pm 2.49	77.49 \pm 2.15	70.83 \pm 3.09	83.52 \pm 0.01	84.23 \pm 1.30
Mean	84.71 \pm 1.56	39.83 \pm 1.58	72.77 \pm 2.77	65.30 \pm 1.99	77.77 \pm 2.66	77.49 \pm 1.36

1223

1224

1225

1226

1227

Table 11: Class-wise F1 scores for Instancenorm layer on datasets balanced @ 400.

Dataset	Wake	N1	N2	N3	REM	F1
ABC	86.46 \pm 1.75	54.45 \pm 0.78	75.68 \pm 2.16	70.75 \pm 0.51	88.60 \pm 0.75	78.36 \pm 1.20
CCSHS	95.69 \pm 0.14	49.23 \pm 2.62	85.29 \pm 0.89	85.98 \pm 0.68	89.23 \pm 0.91	88.73 \pm 0.52
CFS	94.95 \pm 0.19	44.97 \pm 1.34	83.30 \pm 0.60	77.17 \pm 0.39	87.45 \pm 0.38	87.62 \pm 0.27
CHAT	77.67 \pm 6.38	29.47 \pm 8.45	48.78 \pm 6.21	71.34 \pm 2.64	74.58 \pm 1.83	64.19 \pm 4.63
HOMEPA	86.27 \pm 0.53	43.19 \pm 1.46	75.19 \pm 1.07	58.39 \pm 1.03	83.44 \pm 0.46	77.66 \pm 0.58
MASS	67.25 \pm 1.95	43.19 \pm 2.05	78.64 \pm 1.76	65.78 \pm 1.37	78.34 \pm 1.18	76.94 \pm 1.12
MROS	94.80 \pm 0.18	41.46 \pm 0.71	74.42 \pm 1.16	48.89 \pm 2.31	82.11 \pm 0.10	83.95 \pm 0.53
PhysioNet	89.43 \pm 0.41	44.35 \pm 0.62	68.91 \pm 2.82	51.05 \pm 1.32	77.35 \pm 0.95	73.84 \pm 0.93
SHHS	88.62 \pm 0.30	33.02 \pm 2.26	74.31 \pm 2.07	64.28 \pm 0.72	80.32 \pm 0.42	79.12 \pm 0.96
SOF	94.42 \pm 0.20	37.18 \pm 2.37	78.43 \pm 1.88	72.39 \pm 1.56	86.82 \pm 0.70	85.50 \pm 0.86
Mean	87.55 \pm 1.20	42.05 \pm 2.27	74.29 \pm 2.06	66.60 \pm 1.25	82.83 \pm 0.77	79.59 \pm 1.16

1239

1240

1241

1242

1243

1244

Table 12: Class-wise F1 scores for TMA preprocessing with $f = 5$ on datasets balanced @ 400.

1245

Dataset	Wake	N1	N2	N3	REM	F1
ABC	85.50 \pm 0.93	54.76 \pm 0.88	78.91 \pm 1.27	71.40 \pm 1.23	88.43 \pm 0.47	79.49 \pm 0.68
CCSHS	95.51 \pm 0.31	48.72 \pm 2.07	85.02 \pm 1.09	85.37 \pm 1.33	89.33 \pm 0.29	88.47 \pm 0.62
CFS	94.75 \pm 0.26	43.28 \pm 2.27	83.06 \pm 0.79	77.38 \pm 0.28	87.17 \pm 0.36	87.37 \pm 0.44
CHAT	80.70 \pm 4.88	37.51 \pm 1.85	58.89 \pm 4.08	75.71 \pm 2.09	75.95 \pm 2.35	69.90 \pm 2.74
HOMEPA	84.13 \pm 0.98	43.92 \pm 0.51	74.83 \pm 1.40	57.94 \pm 1.19	81.58 \pm 0.13	76.83 \pm 0.97
MASS	70.45 \pm 7.07	41.83 \pm 3.63	77.30 \pm 1.48	65.04 \pm 2.01	79.50 \pm 2.42	76.32 \pm 0.36
MROS	94.50 \pm 0.32	41.74 \pm 1.13	75.20 \pm 1.26	48.92 \pm 2.07	82.35 \pm 0.70	84.15 \pm 0.46
PhysioNet	89.40 \pm 0.50	44.65 \pm 2.19	71.13 \pm 5.36	51.61 \pm 3.94	80.06 \pm 1.02	75.24 \pm 2.72
SHHS	88.30 \pm 0.58	32.95 \pm 2.17	73.23 \pm 2.58	62.33 \pm 0.33	79.27 \pm 0.84	78.19 \pm 0.90
SOF	93.69 \pm 0.34	37.85 \pm 2.16	79.33 \pm 1.49	72.46 \pm 1.92	86.83 \pm 0.29	85.56 \pm 0.90
Mean	87.69 \pm 1.62	42.72 \pm 1.89	75.69 \pm 2.08	66.82 \pm 1.64	83.05 \pm 0.89	80.15 \pm 1.08

1258

1259

1260

1261

1262

Table 13: Class-wise F1 scores for PSDNorm layer with $f = 5$ on datasets balanced @ 400.

1263

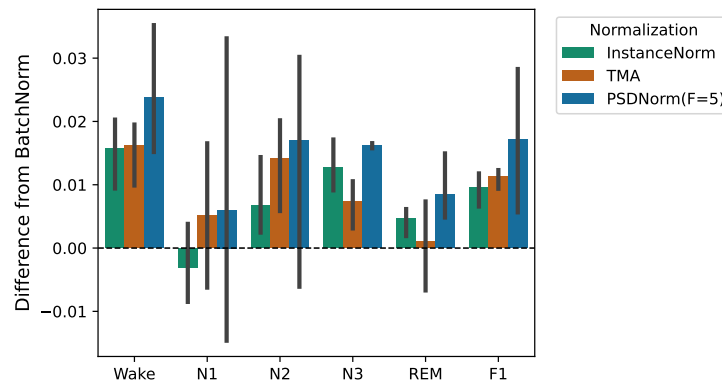
Dataset	Wake	N1	N2	N3	REM	F1
ABC	84.57 \pm 1.39	54.46 \pm 0.59	75.94 \pm 1.14	70.73 \pm 1.00	88.19 \pm 0.23	78.08 \pm 0.78
CCSHS	95.76 \pm 0.21	47.97 \pm 1.71	85.34 \pm 1.76	86.17 \pm 2.24	89.71 \pm 0.33	88.79 \pm 0.99
CFS	95.01 \pm 0.17	42.92 \pm 1.06	82.08 \pm 1.88	76.98 \pm 0.96	87.31 \pm 0.13	87.06 \pm 0.77
CHAT	82.93 \pm 1.99	36.59 \pm 6.79	61.84 \pm 2.98	77.06 \pm 1.32	78.01 \pm 1.62	71.86 \pm 0.95
HOMEPA	85.75 \pm 1.45	44.47 \pm 0.78	75.54 \pm 1.72	58.70 \pm 1.40	83.24 \pm 0.55	77.85 \pm 1.29
MASS	72.74 \pm 2.12	42.20 \pm 1.16	78.56 \pm 2.98	66.13 \pm 2.37	78.23 \pm 3.21	77.16 \pm 1.73
MROS	94.63 \pm 0.31	41.40 \pm 1.64	73.33 \pm 1.80	47.56 \pm 2.25	82.52 \pm 0.47	83.51 \pm 0.84
PhysioNet	89.48 \pm 0.44	44.33 \pm 1.43	67.67 \pm 6.16	49.37 \pm 4.91	79.23 \pm 1.21	73.51 \pm 3.05
SHHS	89.09 \pm 0.66	33.78 \pm 2.53	74.15 \pm 2.70	64.40 \pm 0.29	80.24 \pm 1.03	79.26 \pm 1.35
SOF	93.74 \pm 0.27	34.70 \pm 2.45	76.58 \pm 2.97	70.20 \pm 2.02	85.50 \pm 1.63	84.14 \pm 1.05
Mean	88.37 \pm 0.90	42.28 \pm 2.01	75.10 \pm 2.61	66.73 \pm 1.88	83.22 \pm 1.04	80.12 \pm 1.28

1276

1277

1278

1279



1292

1293

1294

Figure 9: Class-wise F1 score differences between normalization layers for dataset balanced @ 400. The variance is given by the seeds.

1295

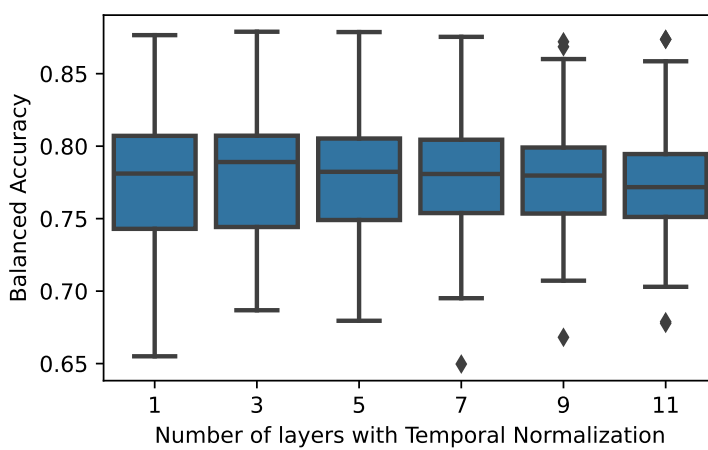


Figure 10: Impact of the number of layers in U-Sleep using PSDNorm with $f = 5$. The BACC score is plotted against the number of layers. The variance is one the Datasets.

Table 14: Performance of different normalization layers in U-Sleep in very low data regime on datasets balanced @ 40.

Dataset	BatchNorm	LayerNorm	InstanceNorm	PSDNorm($f=5$)	PSDNorm($f=15$)
ABC	73.83\pm1.80	64.54 \pm 3.46	72.29 \pm 1.50	71.35 \pm 1.15	72.61 \pm 1.84
CCSHS	83.58 \pm 0.45	77.91 \pm 1.59	85.33\pm0.69	85.10 \pm 0.17	85.00 \pm 0.25
CFS	81.13 \pm 0.85	76.57 \pm 1.89	81.59 \pm 0.47	81.79\pm0.82	80.93 \pm 0.13
CHAT	55.74 \pm 2.38	58.42 \pm 1.64	63.38 \pm 5.26	59.66 \pm 0.89	67.86\pm3.59
HOMEPA	74.52 \pm 1.66	72.19 \pm 1.65	76.03 \pm 0.48	76.01 \pm 0.32	76.14\pm1.63
MASS	70.15\pm3.09	64.79 \pm 2.72	66.58 \pm 0.30	69.49 \pm 1.12	68.21 \pm 6.25
MROS	77.12 \pm 0.03	71.76 \pm 2.38	76.59 \pm 0.28	77.19\pm0.38	76.77 \pm 1.30
PhysioNet	71.68 \pm 1.61	69.59 \pm 1.46	72.68 \pm 3.09	73.67\pm0.93	72.08 \pm 3.65
SHHS	73.74 \pm 1.11	71.50 \pm 0.97	75.56 \pm 1.66	75.43 \pm 1.38	76.00\pm0.63
SOF	75.84 \pm 2.16	73.50 \pm 1.97	76.54\pm1.59	75.14 \pm 1.79	76.00 \pm 3.00
Mean	73.35 \pm 0.87	70.72 \pm 1.22	75.19 \pm 1.03	74.79 \pm 0.75	75.88\pm0.93

improving sleep stage classification. But we have to note that for N1 and N2 the variance over the seed is big showing the instability of the training for these classes.

A.14 STUDY OF IMPACT OF NUMBER OF LAYER IN U-SLEEP USING PSDNORM

In the main paper, we apply PSDNorm in 3 layers of U-Sleep. Here, we investigate the impact of varying the number of layers that utilize PSDNorm. Figure 10 shows the BACC score as a function of the number of layers with PSDNorm. The results indicate that increasing the number of layers with PSDNorm reach a plateau after 3 layers, but does reduce the variance across datasets. This suggests that while adding more layers with PSDNorm can enhance performance, there are diminishing returns beyond a certain point. Thus, using PSDNorm in 3 layers strikes a good balance between performance, good variance, and computational efficiency.

A.15 STUDY IN VERY LOW DATA REGIME

In this section, we explore the performance of different normalization layers in U-Sleep when trained on a very limited dataset, specifically balanced @ 40 subjects. The results indicate that in this low data regime, PSDNorm with a small filter size ($F = 5$) struggle to outperform InstanceNorm while still outperforming BatchNorm and LayerNorm. However, PSDNorm with a larger filter size ($F = 15$) gives the best average performance across datasets with an increase of more than 10% in BACC

1350 Table 15: Comparison of PSDNorm with AdaBN on datasets balanced @400 using U-Sleep.
1351

Dataset	BatchNorm	LayerNorm	InstanceNorm	AdaBN(3)	AdaBN(full)	TMA	PSDNorm(F=5)
ABC	78.26 ± 1.33	75.29 ± 0.81	78.73 ± 0.42	78.25 ± 1.30	76.89 ± 1.30	78.04 ± 0.51	78.18 ± 0.68
CCSHS	87.42 ± 0.16	85.20 ± 0.48	87.62 ± 0.42	87.38 ± 0.17	87.02 ± 0.16	87.57 ± 0.20	87.58 ± 0.30
CFS	84.32 ± 0.57	81.66 ± 1.36	84.72 ± 0.33	84.21 ± 0.60	84.05 ± 0.56	84.58 ± 0.20	84.29 ± 0.36
CHAT	66.55 ± 0.88	61.19 ± 1.16	64.43 ± 4.41	66.49 ± 0.89	66.44 ± 0.88	68.73 ± 2.48	70.28 ± 1.70
HOMEPA	75.25 ± 0.50	74.86 ± 0.25	76.47 ± 0.63	75.15 ± 0.46	74.46 ± 0.53	76.10 ± 0.32	76.83 ± 0.61
MASS	70.00 ± 1.91	68.56 ± 3.33	71.52 ± 1.13	69.68 ± 1.66	68.31 ± 1.86	71.63 ± 1.92	72.77 ± 1.09
MROS	80.37 ± 0.20	78.05 ± 0.22	80.28 ± 0.21	80.34 ± 0.20	80.27 ± 0.20	80.09 ± 0.40	80.26 ± 0.11
PhysioNet	75.81 ± 0.13	71.82 ± 2.12	74.68 ± 0.55	75.27 ± 0.14	74.01 ± 0.14	75.31 ± 1.54	74.82 ± 2.11
SHHS	76.44 ± 0.92	75.12 ± 0.39	78.68 ± 0.37	76.43 ± 0.92	76.41 ± 0.92	77.00 ± 0.39	78.88 ± 0.68
SOF	81.08 ± 1.14	78.70 ± 0.50	80.68 ± 1.38	81.05 ± 1.13	80.67 ± 1.13	81.25 ± 0.71	79.49 ± 0.41
Mean	77.22 ± 0.34	75.04 ± 0.42	78.17 ± 0.28	77.18 ± 0.34	77.08 ± 0.34	77.74 ± 0.36	78.85 ± 0.59

1362
1363 compared to other normalization layers for CHAT dataset. This suggests that in scenarios with very
1364 limited data, stronger normalization (larger filter size) is beneficial to prevent overfitting and enhance
1365 generalization.
1366

1367 A.16 COMPARISON WITH ADABN 1368

1369 Table 15 presents a comparison between PSDNorm and AdaBN using the U-Sleep architecture on
1370 datasets balanced @400. AdaBN adapts the BatchNorm statistics separately for each subject. In the
1371 original paper, all BN layers are replaced (AdaBN(full)), but for a fair comparison we also evaluate
1372 one additional settings: AdaBN(3), which adapts only the first three BN layers.
1373

1374 As expected, AdaBN struggles to achieve strong performance on sleep staging. It consistently
1375 underperforms compared to TMA and, in some cases, even performs worse than standard BatchNorm.
1376 Notably, increasing the number of adapted BN layers further degrades performance, highlighting the
1377 importance of not adapting too many layers within the model. In contrast, PSDNorm consistently
1378 outperforms AdaBN across all datasets, demonstrating its effectiveness in normalizing features for
1379 sleep staging tasks.
1380
1381
1382
1383
1384
1385
1386
1387
1388
1389
1390
1391
1392
1393
1394
1395
1396
1397
1398
1399
1400
1401
1402
1403